

TEMPORAL DIFFERENCE LEARNING WITH CONSTRAINED INITIAL REPRESENTATIONS

Jiafei Lyu¹, Jingwen Yang², Zhongjian Qiao¹, Runze Liu¹, Zeyuan Liu¹, Deheng Ye²,
 Zongqing Lu³, Xiu Li¹

¹Tsinghua Shenzhen International Graduate School, Tsinghua University

²Tencent, ³School of Computer Science, Peking University

dmksjfl@gmail.com, li.xiu@sz.tsinghua.edu.cn

ABSTRACT

Recently, there have been numerous attempts to enhance the sample efficiency of off-policy reinforcement learning (RL) agents when interacting with the environment, including architecture improvements and new algorithms. Despite these advances, they overlook the potential of directly constraining the initial representations of the input data, which can intuitively alleviate the distribution shift issue and stabilize training. In this paper, we introduce the Tanh function into the initial layer to fulfill such a constraint. We theoretically unpack the convergence property of the temporal difference learning with the Tanh function under linear function approximation. Motivated by theoretical insights, we present our Constrained Initial Representations framework, tagged CIR, which is made up of three components: (i) the Tanh activation along with normalization methods to stabilize representations; (ii) the skip connection module to provide a linear pathway from the shallow layer to the deep layer; (iii) the convex Q-learning that allows a more flexible value estimate and mitigates potential conservatism. Empirical results show that CIR exhibits strong performance on numerous continuous control tasks, even being competitive or surpassing existing strong baseline methods.

1 INTRODUCTION

Conventional practice that aims at enhancing the sample efficiency of the reinforcement learning (RL) agent mainly focuses on algorithmic improvement, such as addressing the value overestimation issue (Fujimoto et al., 2018; Kuznetsov et al., 2020), improving the exploration (Haarnoja et al., 2018; Ladosz et al., 2022; Yang et al., 2024) or exploitation (Chen et al., 2021; D’Oro et al., 2023) capability of the agent, alleviating the primacy bias (Nikishin et al., 2022), leveraging model-based approaches (Buckman et al., 2018; Fujimoto et al., 2023; 2025) for planning (Hansen et al., 2022; 2024) or data augmentation (Voelcker et al., 2025), etc. Interestingly, these studies often rely on a small and simple network architecture (vanilla MLP in most cases). It appears that the RL community has long exhibited a preference for algorithmic refinement rather than architectural innovation. Recently, there have been some valuable attempts in scaling up RL algorithms and found that simply scaling up network capacity can degrade performance (Andrychowicz et al., 2020). BRO (Nauman et al., 2024) first successfully scales up network capacity and replay ratios by introducing strong regularization techniques, optimistic exploration, and distributional Q-learning (Bellemare et al., 2017). Furthermore, SimBa (Lee et al., 2025a) modifies the network architecture by injecting a simplicity bias and acquires strong performance across diverse domains.

Different from these advances, we provide a novel perspective to improve the sample efficiency, i.e., *directly constraining the input representations*. To that end, we incorporate the Tanh function into the initial layer of the network. This enjoys several advantages: (i) the Tanh function is increasing and order-preserving and does not change the sign of the representations; (ii) the Tanh function constrains the element to lie between -1 and 1 , ensuring value stabilization; (iii) it is easy to compute its gradient. The Tanh function can also help alleviate the severe distribution shift caused by OOD input samples, as illustrated in Figure 1. To better support our claim, we consider a two-layer MLP network $y = W_2(\sigma(W_1 x))$, where we omit the bias term for simplicity, $x \in \mathbb{R}^d$ is the input vector, $W_1 \in \mathbb{R}^{h \times d}$, $W_2 \in \mathbb{R}^{1 \times h}$ are weight matrices, $\sigma(\cdot)$ denotes the activation function, h is the

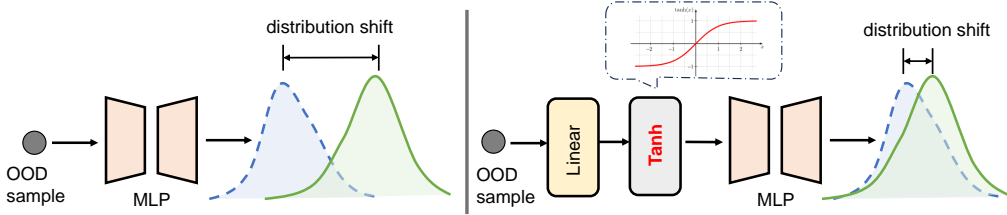


Figure 1: **Illustration of our motivation.** When encountering the out-of-distribution (OOD) sample that deviates *far* from the distribution of the current policy, the vanilla MLP network may incur severe distribution shift issue (**left**) while after adding the Tanh activation to the MLP, the negative influence of the OOD sample can be mitigated (**right**).

hidden dimension, d is the input dimension. If $\sigma(\cdot) = \text{ReLU}(\cdot)$, then given the input x_1 and x_2 , the output deviation gives $|y_1 - y_2| \leq \|W_2\|_F \cdot \|W_1\|_F \cdot \|x_1 - x_2\|_F$, where $\|\cdot\|_F$ is the Frobenius norm. Unfortunately, the above upper bound is *unconstrained* and can be large if x_2 deviates far from x_1 (this can often happen due to exploration and evolving policy). If $\sigma(\cdot) = \tanh(\cdot)$, we similarly have $|y_1 - y_2| \leq \|W_2\|_F \cdot \|\tanh(W_1 x_1) - \tanh(W_1 x_2)\|_F$. Since $|\tanh(x)| \leq 1$, the upper bound here can always be bounded regardless of how x_2 differs from x_1 (the output will not change drastically). That being said, the negative influence of the potential OOD samples can be mitigated.

To further show the benefits of using the Tanh function, we conduct theoretical analysis on temporal difference (TD) learning with the Tanh function under linear function approximation. Our results show that the linear independence between basis functions can still hold after using the Tanh function. Another exciting finding is that incorporating the Tanh function can reduce the variance of the gradient of the least square TD (LSTD) objective function, which validates that the Tanh function can stabilize training. Furthermore, we show that TD(0) can still converge to a fixed point after adding the Tanh function and the global convergence can be guaranteed by adding regularizations. These theoretical results pave the way for applying the proposed idea to the DRL setting.

As a result, we propose the Constrained Initial Representations algorithm, namely CIR. It mainly contains three key components: (i) the representation constraint module that leverages the Tanh function, the average representation normalization and layer normalization (Ba et al., 2016) to stabilize representations and mitigate the possible gradient vanishing issue; (ii) the skip connection module that maintains a direct information pathway from the shallow layer to the deep layer to better pass information; (iii) the convex Q-learning that permits better value estimate and mitigates the risk of conservatism from Tanh. These components are novel and feature distinct ways of achieving high sample efficiency compared to previous methods. We evaluate CIR on DMC suite (Tassa et al., 2018), HumanoidBench (Sferrazza et al., 2024) and ODRL (Lyu et al., 2024c) tasks. The experimental results show that CIR can match or even outperform recent strong baseline methods on numerous tasks. To facilitate reproducibility, we include our codes in the supplemental materials.

2 RELATED WORK

Regularization in DRL. Introducing implicit or explicit regularization terms has been well-explored in other fields (Tang et al., 2018; Xu et al., 2015; Xie et al., 2016; Xin et al., 2021; Merity et al., 2017). In DRL, there are also many studies that add new regularization terms into the critic or the actor network to stabilize training, including regularizing the uncertainty of value estimate (Lyu et al., 2022; Eysenbach et al., 2023), penalizing the TD error of the critic (Parisi et al., 2018; Shao et al., 2022), involving action gradient regularization (Kostrikov et al., 2021; D’Oro & Jaśkowski, 2020; Li et al., 2022), divergence regularization (Su & Lu, 2021), mutual information regularization (Leibfried & Grau-Moya, 2019), etc. Besides, regularization techniques from supervised learning are also widely adopted in DRL to alleviate the overfitting issue, e.g., normalization tricks (Ba et al., 2016; Gogianu et al., 2021; Bjorck et al., 2021; Bhatt et al., 2024; Lee et al., 2025a;b; Palenicek et al., 2025; Elsayed et al., 2024), dropout (Srivastava et al., 2014; Wu et al., 2021; Hiraoka et al., 2021), weight decay (Farebrother et al., 2018; Nauman et al., 2024), etc. Moreover, some researchers resort to reinitialization approaches to escape from the local optima and boost the sample efficiency of the agent, e.g., resetting the parameters to their initial distributions (Nikishin et al., 2022; Qiao et al.,

2024), selectively reinitializing dormant weights (Sokar et al., 2023), combining current weights with random weights (Schwarzer et al., 2023; Xu et al., 2024). In contrast, our CIR framework directly regularizes the *initial representations* of the transition sample.

Sample-efficient RL algorithms. A long-standing goal in DRL is to enable the agent to quickly acquire strong continuous control policies with a small budget of data from the environment (Yu, 2018; Du et al., 2019). To fulfill that, some researchers enhance the sample efficiency by improving the exploration ability of the agent (Asmuth et al., 2012; Still & Precup, 2012; Burda et al., 2018; Haarnoja et al., 2018; Ladosz et al., 2022; Yang et al., 2024; Jiang et al., 2025), reducing value estimation bias (Van Hasselt et al., 2016; Fujimoto et al., 2018; Kuznetsov et al., 2020; Moskovitz et al., 2021; Lyu et al., 2022; 2023), using new experience replay methods (Fujimoto et al., 2020; Schaul et al., 2015; Andrychowicz et al., 2017), increasing the frequency of data reuse (Chen et al., 2021; D’Oro et al., 2023; Lyu et al., 2024b; Romeo et al., 2025), injecting representation learning objectives (De Bruin et al., 2018; Ota et al., 2020; Laskin et al., 2020; Fujimoto et al., 2023; Yan et al., 2024; Fujimoto et al., 2025), leveraging model-based approaches (Janner et al., 2019; Buckman et al., 2018; Hansen et al., 2022; Hafner et al., 2023; Hansen et al., 2024; Voelcker et al., 2025), etc. The above research can be categorized into algorithmic improvement. Another line of studies focuses on architecture improvement, which has been widely studied in computer vision (CV) (He et al., 2015; Targ et al., 2016; Goodfellow et al., 2021; Ho et al., 2020) and natural language processing (NLP) (Vaswani et al., 2017; Devlin et al., 2019; Beck et al., 2024). BRO (Nauman et al., 2024) empirically shows that architecture modification can incur strong performance improvement, breaking the curse that simply scaling network capacity can degrade performance (Andrychowicz et al., 2020). Moreover, the SimBa architecture (Lee et al., 2025a) outperforms BRO by incorporating simplicity bias into the network design. Compared to these studies, our CIR method also modifies the network architecture with a Tanh function to stabilize representations.

3 PRELIMINARIES

Reinforcement learning (RL) problems can be formulated by the tuple $(\mathcal{S}, \mathcal{A}, r, \gamma, P)$, where \mathcal{S} is the state space, \mathcal{A} is the action space, $r(s, a) : \mathcal{S} \times \mathcal{A} \rightarrow \mathbb{R}$ is the scalar reward signal, $\gamma \in [0, 1]$ is the discount factor, $P(s'|s, a)$ is the transition probability. In online RL, the agent continually interacts with the environment using a policy $\pi_\psi(\cdot|s)$ parameterized by ψ . The goal of the agent is to maximize the expected cumulative discounted rewards: $\max J(\psi) = \mathbb{E}[\sum_{t=0}^{\infty} \gamma^t r(s_t, a_t)|s_0, a_0; \pi]$. We have the state-action value function $Q^\pi(s, a) := \mathbb{E}_\pi[\sum_{t=0}^{\infty} \gamma^t r(s_t, a_t)|s_0 = s, a_0 = a]$, the value function $V^\pi(s) := \mathbb{E}_\pi[\sum_{t=0}^{\infty} \gamma^t r(s_t, a_t)|s_0 = s]$.

For theoretical analysis, we assume that the MDP has finite state space and action space with size S and A , and the Markov chain in this MDP has a stationary distribution ν and is ergodic. We consider linear function approximation (Tsitsiklis & Van Roy, 1996; Bhandari et al., 2018; Jin et al., 2020; Zou et al., 2019), where the value function V^π is a linear combination of features, $V(s; \theta) = \phi(s)^\top \theta$, where $\phi : \mathcal{S} \rightarrow \mathbb{R}^d$ is a known feature map, θ is the weight vector. We similarly have the state-action value function $Q(s, a; \theta) = \psi(s, a)^\top \theta$, $\psi : \mathcal{S} \times \mathcal{A} \rightarrow \mathbb{R}^d$ is the feature map. We focus on V for convenience and consider the TD(0) update rule, which is given by

$$\theta_{t+1} \leftarrow \theta_t + \alpha_t (r_t + \gamma \phi(s_{t+1})^\top \theta_t - \phi(s_t)^\top \theta_t) \phi(s_t), \quad (1)$$

where α_t is the step size at timestep t . We then introduce per-element Tanh function to the feature and have $V(s; \theta) = \tanh(W\phi(s))^\top \theta$, where $W \in \mathbb{R}^{d \times d}$ is a positive definite diagonal constant matrix. Similarly, we have the TD(0) update rule after introducing tanh,

$$\theta_{t+1} \leftarrow \theta_t + \alpha_t (r_t + \gamma \tanh(W\phi(s_{t+1}))^\top \theta_t - \tanh(W\phi(s_t))^\top \theta_t) \tanh(W\phi(s_t)). \quad (2)$$

Without loss of generality, we assume that the rewards are bounded, $\forall s, a, |r(s, a)| \leq r_{\max}$. Given a positive definite matrix D , we denote $\|x\|_D = \sqrt{x^\top D x}$ as the vector norm induced by D . For simplicity, we denote $\|\cdot\| = \|\cdot\|_I$, where I is the identity matrix.

4 THEORETICAL ANALYSIS

In this section, we theoretically analyze the benefits of incorporating the Tanh function for representation stabilization and convergence properties in temporal difference learning. We conduct

theoretical analysis under linear function approximation since it can be difficult to analyze its theoretical properties when involving neural networks. Due to space limit, all proofs are deferred to Appendix A. We first impose the following assumption, which is widely adopted in previous literature (Tsitsiklis & Van Roy, 1996; Jin et al., 2020; Zhang et al., 2023).

Assumption 4.1. *The feature matrix $\phi = [\phi_1, \phi_2, \dots, \phi_S]^\top$ has full column rank, i.e., the basis functions $\{\phi_k | k = 1, \dots, S\}$ are linearly independent.*

The above assumption is critical for convergence analysis. We show in Theorem 4.2 that this property still holds for the feature matrix after applying the Tanh function by properly choosing W .

Theorem 4.2 (Linear Independence). *Suppose that $W = c \cdot I$, where $c \in \mathbb{R}$ is a sufficient small positive number, I is the identity matrix, then if basis functions $\{\phi_1, \dots, \phi_S\}$ are linearly independent, then the transformed basis functions $\{\tanh(W\phi_1), \dots, \tanh(W\phi_S)\}$ are also linearly independent.*

Furthermore, we show in the following theorem that the constrained features can incur a smaller gradient variance compared to its unconstrained counterpart.

Theorem 4.3 (Variance Reduction). *Given any s , suppose the feature $\phi(s)$ follows a distribution with $\mathbb{E}[\phi(s)] = 0$. Consider per-transition least square TD (LSTD) objective $\mathcal{L} = \frac{1}{2}[(r + \gamma V(s'; \theta) - V(s; \theta))^2]$, then if $V(s; \theta) = \phi(s)^\top \theta$, the variance of the semi-gradient term satisfies:*

$$\|\text{Var}(\nabla_\theta \mathcal{L})\| \leq (r_{\max} + (1 + \gamma)\|\theta\|\Lambda)^2 \cdot \|\phi(s)\|^2, \quad (3)$$

where $\Lambda = \max\{\|\phi(s)\|, \|\phi(s')\|\}$. While if $V(s; \theta) = \tanh(W\phi(s))^\top \theta$, we have

$$\|\text{Var}(\nabla_\theta \mathcal{L})\| \leq (r_{\max} + (1 + \gamma)\|\theta\|\lambda_W \Lambda)^2 \cdot \|\tanh(W\phi(s))\|^2, \quad (4)$$

where λ_W is the maximum eigenvalue of W .

Remark. By properly choosing the constant matrix W , the upper bound of the variance term with the Tanh function can be smaller than the upper bound of the vanilla variance term. For example, by setting $W = I$ (identity matrix), $\tanh(W\phi(s)) = \tanh(\phi(s))$, $\lambda_W = 1$, then we have

$$(r_{\max} + (1 + \gamma)\|\theta\|\lambda_W \Lambda)^2 \cdot \|\tanh(\phi(s))\|^2 \leq (r_{\max} + (1 + \gamma)\|\theta\|\Lambda)^2 \cdot \|\phi(s)\|^2,$$

where we use the fact that $|x| \geq |\tanh(x)|, \forall x$. That is, if one chooses $W = c \cdot I, c \in \mathbb{R}, c \in (0, 1)$, the upper bound after using Tanh is always tighter. It indicates that Tanh *can stabilize the training process and incur smaller gradient variance*. Note that we do not make any specific assumptions on $\|\phi\|$ since the Tanh function enforces an inherent constraint on the features. Since $|\tanh(x)| \leq 1, \forall x$, we have $\|\tanh(W\phi(s))\| \leq \sqrt{d}$, then the variance upper bound can be simplified,

$$\|\text{Var}(\nabla_\theta \mathcal{L})\| \leq (r_{\max} + (1 + \gamma)\|\theta\|\sqrt{d})^2 \cdot d. \quad (5)$$

We then formally show that TD(0) with linear function approximation and Tanh feature transformation is guaranteed to converge to a fixed point.

Theorem 4.4 (Convergence under TD(0)). *Consider the TD(0) update rule for the value function $V(s; \theta) = \tanh(W\phi(s))^\top \theta$. Suppose we project the parameters θ onto bounded sets $\Theta = \{\theta | \|\theta\|_2 \leq C_\theta\}$ after each update. If the step sizes satisfy $\sum \alpha_t = \infty$, $\sum \alpha_t^2 < \infty$, then the projected TD(0) algorithm converges almost surely to a fixed point θ^* .*

However, the above theorem can only ensure that the weight converges to a fixed point. It remains unclear whether it can converge to a global optimum. We then introduce the regularized optimization objective and show that θ converges to a unique global minima θ^* .

Theorem 4.5 (Global Convergence under Regularization). *Given the regularized loss $\mathcal{L}(\theta) = \mathbb{E}[(r + \gamma \tanh(W\phi(s'))^\top \theta - \tanh(W\phi(s))^\top \theta)^2] + \lambda_\theta \|\theta\|_2^2$, assume that (a) the step size α is a constant; (b) the gradient of the loss $\mathcal{L}(\theta)$ is β -smooth, i.e., $\|\nabla \mathcal{L}(\theta_1) - \nabla \mathcal{L}(\theta_2)\| \leq \beta \|\theta_1 - \theta_2\|$; (c) the regularization parameter satisfies $0 < \lambda_\theta < \frac{\beta}{2}$. Then, gradient descent with step size $\alpha \leq 1/\beta$ converges linearly to a unique global minimum θ^* .*

In summary, the above theoretical results generally describe the variance reduction capability and the convergence results after applying the Tanh function on features, which sheds light on extending this simple idea into the DRL scenario.

5 ALGORITHM

Motivated by the theoretical results, we formally present our CIR framework, which mainly comprises three parts: (i) a Tanh function and two normalization techniques to stabilize representations; (ii) the skip connection module that combines information from shallow layers and deep layers; (iii) a convex Q-learning approach to further enhance the performance of the agent.

5.1 CONSTRAINING INITIAL REPRESENTATION WITH THE Tanh ACTIVATION

Our focus is on state-based continuous control tasks, where plain MLP networks are commonly used. However, it can be fragile to samples that deviate far from the current distribution (as analyzed in Section 1). To stabilize training, we add a Tanh function to the initial layer of the network. We do not place the Tanh function in the middle layer or deep layers because (i) the latter layers can be naturally regularized if the initial representations are constrained, since the magnitude of the input representations are controlled, and (ii) it may be challenging for the gradient to backpropagate and the gradient may vanish before the initial layers can be well-updated.

Nevertheless, naively utilizing the Tanh function can incur gradient vanishing issue (Wang et al., 2019; Goodfellow et al., 2016), e.g., given the input vector $\mathbf{o}_t \in \mathbb{R}^d$ at timestep t , if the initial representations $\mathbf{x}_t = \text{Linear}(\mathbf{o}_t) \in \mathbb{R}^h$ have large values (i.e., $\text{tanh}(\mathbf{x}_t) \approx [1, 1, \dots, 1]$), its gradient after applying the Tanh function can be small, $\nabla \text{tanh}(\mathbf{x}_t) \approx \mathbf{0}$ (since $\nabla \text{tanh}(x) = 1 - (\text{tanh}(x))^2$). To mitigate this concern, we need to manually compress the representations to ensure that they do not lie in the gradient vanishing region of Tanh . A natural idea is to weight the initial representations with a small constant c (this can be seen as setting the weight matrix $W = c \cdot I$ in our theoretical analysis). However, this approach lacks flexibility because different environments possess different state space and action space dimensions, dynamics transition probability, and reward scales. One may need to grid search the best c per task, which can be labor-intensive and expensive. Instead, we introduce the average representation normalization trick (AvgRNorm) to adaptively control the representations from different tasks without tuning the parameter c ,

$$\text{AvgRNorm}(\mathbf{x}) = c \times \frac{\mathbf{x}}{\text{Mean}(\tilde{\mathbf{x}})}, \quad \tilde{\mathbf{x}} = |\mathbf{x}|, \quad (6)$$

where $\text{Mean}(\cdot)$ is the mean operator, c is a small positive number that controls the scale of the normalized representations (as required in Theorem 4.2). We use the absolute values of representations to avoid $\text{Mean}(\tilde{\mathbf{x}}) \approx 0$. AvgRNorm can effectively bound representations and decrease the gradient contribution of those large values in representations. We adopt $c = 0.1$ by default.

Furthermore, based on Theorem 4.5, additional regularization terms are needed to acquire global convergence. Since regularizing the parameters is inherently equivalent to regularizing the representations, we further regularize representations for better stability by involving layer normalization, which is proven effective in prior works (Lee et al., 2025a; Nauman et al., 2024). Finally, the constrained initial representation is given by,

$$\mathbf{z}_t = \text{tanh}(\text{AvgRNorm}(\text{LayerNorm}(\text{Linear}(\mathbf{o}_t)))). \quad (7)$$

5.2 BOOSTING GRADIENT FLOW WITH SKIP CONNECTIONS

After the initial representations are constrained, we feed forward them to downstream layers. Built upon previous findings that scaling aids sample efficiency (Nauman et al., 2024; Lee et al., 2025a;b), we also scale up the critic networks by expanding the depth and width of the critic networks. To better facilitate gradient propagation, we utilize the skip connection technique (Ronneberger et al., 2015; Milletari et al., 2016), which is less explored in DRL. That indicates that we adopt a U-shape network, which contains a down-sampling path to capture features, and a symmetric up-sampling path to aggregate features from shallow layers and deep layers. Different from prior works, we do not expand the channel of the features during the process of either down-sampling or up-sampling, and we fuse shallow and deep abstract representations through linear addition rather than concatenation.

We still adopt layer normalization for stabilizing representations in the latter layers (which can be seen as the regularization term in Theorem 4.5). Formally, for the down-sampling layers $l \in \{1, \dots, L\}$, with the number of layers L , its representations at timestep t is given by,

$$\mathbf{x}_t^l = \text{LayerNorm}(\text{Linear}(\mathbf{x}_t^{l-1})), \quad (8)$$

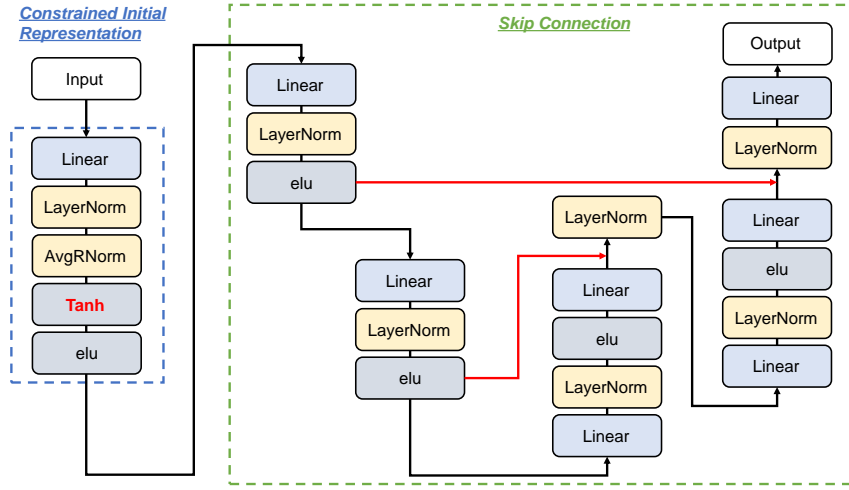


Figure 2: **Architecture overview of CIR.** CIR adopts (a) the AvgRNorm module and the Tanh activation to stabilize initial representations; (b) skip connection modules to facilitate gradient flow.

where $\mathbf{x}_t^0 = \mathbf{z}_t$ is the initial constrained representation calculated via Equation 7. For a symmetric up-sampling layer $l \in \{1, \dots, L\}$, its representation is calculated by linear addition, i.e.,

$$\mathbf{x}_t^{2L-l+1} = \mathbf{x}_t^l + \text{Linear}(\text{LayerNorm}(\text{Linear}(\mathbf{x}_t^{2L-l}))). \quad (9)$$

This resembles residual learning (He et al., 2015). Note that we omit the activation function terms in Equation 8 and Equation 9 for clarity (we use the elu activation function). There are two reasons for adopting the skip connection technique. First, the U-shape network with skip connections enables effective multi-scale feature extraction, facilitating both global feature understanding and local information preservation. Second, it combines shallow low-level information with deep abstract representations, which enables model scaling and eases gradient vanishing. It also enhances the representational capacity of the model. Meanwhile, we do not involve modules like convolution layers or pooling. The detailed network architecture is shown in Figure 2. We use 2 down-sampling and up-sampling layers by default ($\approx 3M$ parameters). We adopt the vanilla MLP network for the actor since we find that modifying network architecture or scaling the actor network is less effective, which matches the results in BRO (Nauman et al., 2024).

5.3 CONVEX Q-LEARNING

Following our theoretical results, we adopt the TD(0)-style update rule for training critic networks. Denote $Q_{\theta_1}(s, a), Q_{\theta_2}(s, a)$ as the critic networks parameterized by θ_1, θ_2 , respectively, $\pi_\phi(\cdot|s)$ as the actor network parameterized by ϕ , the objective function of TD(0) with clipped double Q-learning (CDQ) gives $\mathcal{L}(\theta_i) = \mathbb{E}_{(s, a, r, s') \sim \rho}[(y - Q_{\theta_i}(s, a))^2]$, where $y = r + \gamma(\min_{j \in \{1, 2\}} Q_{\theta'_j}(s', a') - \alpha \log \pi_\phi(a'|s'))$ is the target value, $\theta'_j, j \in \{1, 2\}$ are target network parameters, $a' \sim \pi_\phi(\cdot|s)$, ρ is the sample distribution in the replay buffer, α is the temperature coefficient. Existing studies show that CDQ can incur underestimation bias (i.e., conservatism) (Ciosek et al., 2019; Pan et al., 2020; Lyu et al., 2022). Meanwhile, constraining initial representations with Tanh can be conservative since it constrains the initial representations and the output of the model. Eventually, the conservatism may be excessive if we use CDQ in CIR.

To mitigate the potential negative influence of conservatism from the architecture, we propose a convex Q-learning approach to encourage the learned value function to be optimistic. In convex Q-learning, we modify the target value by combining the minimum and maximum of value functions,

$$y = r(s, a) + \gamma \left(\lambda \times \min_{i \in \{1, 2\}} Q_{\theta'_i}(s', a') + (1 - \lambda) \times \max_{i \in \{1, 2\}} Q_{\theta'_i}(s', a') - \alpha \log \pi_\phi(a'|s') \right). \quad (10)$$

The over-conservatism issue can be eased by properly choosing λ . We set $\lambda = 0.3$ by default. We show below that the convex Q-learning is guaranteed to converge to the optimal value function.

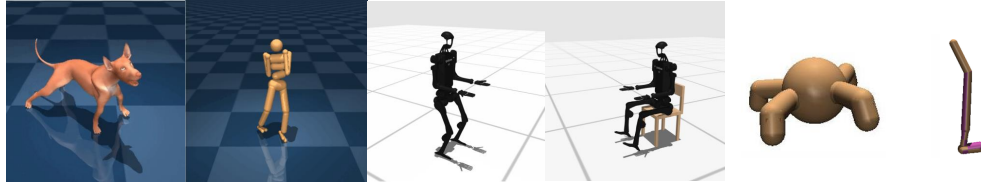


Figure 3: **Visualizations of the benchmarks.** We consider tasks from the DMC suite, HumanoidBench and ODRL for evaluations. These tasks feature varying complexity and can be challenging.

Theorem 5.1. *Under mild assumptions, for any $\lambda \in (0, 1]$, the Convex Q-learning converges to the optimal value function Q^* as defined by the Bellman optimality equation with probability 1.*

We use average Q values for updating the actor following prior works (Chen et al., 2021; Nauman et al., 2024), i.e., $\mathcal{L}(\phi) = \mathbb{E}_{s \sim \rho, \tilde{a} \sim \pi_\phi(\cdot|s)} [\alpha \log \pi_\phi(\tilde{a}|s) - \frac{1}{2} \sum_{j=1,2} Q_{\theta_j}(s, \tilde{a})]$. We further adopt the sample multiple reuse (SMR) (Lyu et al., 2024b) trick that reuses the fixed sampled batch M times to boost sample efficiency, which functions better than other data replay methods.

Putting together all the aforementioned techniques gives birth to our CIR algorithm. We adopt SAC (Haarnoja et al., 2018) as the base algorithm, modifying its critic network architecture and replacing CDQ with the convex Q-learning. The pseudo-code for CIR is available in Appendix B.

6 EXPERIMENTS

In this section, we empirically investigate the applicability of CIR across numerous tasks. Across each domain, we evaluate the performance of CIR under a fixed set of hyperparameters and algorithmic configurations¹. Due to space limits, more empirical results are deferred to Appendix E.

We utilize three continuous control benchmarks for performance evaluation, DMC suite (Tassa et al., 2018), HumanoidBench (Sferrazza et al., 2024) and ODRL (Lyu et al., 2024c), as depicted in Figure 3. We adopt 20 DMC suite easy and medium-level tasks, 7 DMC hard tasks, 14 HumanoidBench locomotion tasks, and 8 ODRL tasks, leading to a total of 49 tasks. Following SimBa (Lee et al., 2025a), we use different training steps per environment based on their complexity, 500K steps for DMC easy and medium tasks, 1M for DMC hard and ODRL tasks, 2M for HumanoidBench tasks. Details on environmental descriptions can be found in Appendix C. Note that in ODRL, there exist dynamics discrepancies between the source domain and the target domain, and the agent needs to acquire good performance in the target domain by using data from both domains. This benchmark is adopted to empirically evaluate CIR’s ability to handle OOD data, as illustrated in Figure 1.

6.1 MAIN RESULTS

We consider the following methods as baselines: **SAC** (Haarnoja et al., 2018), a classical and widely used off-policy maximum entropy RL algorithm; **TD7** (Fujimoto et al., 2023), an enhanced version of TD3 (Fujimoto et al., 2018) by incorporating state-action representation learning; **BRO** (Nauman et al., 2024) that combines critic network scaling with layer normalization and residual layer, optimistic exploration, distributional value modeling, and periodic resets; **DreamerV3** (Hafner et al., 2023), a strong model-based RL algorithm that optimizes a policy via synthetic trajectories; **TD-MPC2** (Hansen et al., 2024) that empowers policy learning by training latent world models and leveraging model predictive control; **SimBa** (Lee et al., 2025a) that directly modifies the network architecture of the agent by combining running statistics normalization (RSNorm), a residual feed-forward block, and post-layer normalization. For a fair comparison, we use BRO-Fast and SimBa with the update-to-data (UTD) ratio 2. We use the SMR ratio $M = 2$ in CIR across all tasks.

For ODRL tasks, we consider the following baselines: **SAC** (Haarnoja et al., 2018), **DARC** (Eysenbach et al., 2021) that train domain classifiers for cross-dynamics policy adaptation, and **PAR** (Lyu et al., 2024a) that fulfill efficient policy adaptation via capturing representation mismatch.

¹Methods like SimBa (Lee et al., 2025a) adopt different algorithmic configurations on different tasks

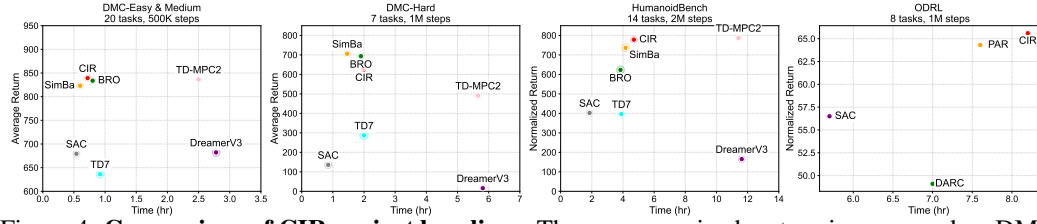


Figure 4: **Comparison of CIR against baselines.** The average episode return is compared on DMC tasks while normalized return results are compared in HumanoidBench and ODRL tasks.

We summarize empirical results in Figure 4, where the x-axis denotes the computation time using an RTX 3090 GPU, and the y-axis represents the aggregated return. Points that approach the upper-left region indicate higher compute efficiency while points in the lower-right region have lower compute efficiency. The shaded region denotes standard deviations. We find that CIR exhibits strong performance on DMC easy and medium tasks, exceeding all baselines. On HumanoidBench tasks, CIR outperforms strong baselines like SimBa, and matches the performance of TD-MPC2. For DMC hard tasks, CIR underperforms SimBa and BRO, but is still better than other baselines. It is evident that CIR can achieve competitive sample efficiency against recent strong model-free methods while not increasing much computation time. CIR is 2 times computationally more efficient compared to model-based methods like TD-MPC2 and DreamerV3. Moreover, CIR exhibits strong performance on ODRL tasks, despite that CIR does not include any special components designed for this setting, indicating its advantages in mitigating the OOD issue and stabilizing training. The empirical results highlight the effectiveness of CIR and the potential of constraining initial representations.

6.2 EXTENDED RESULTS ON COMPLEX TASKS

Though CIR underperforms SimBa on some tasks, it can beat SimBa on complex tasks like HumanoidBench. To further show the effectiveness of CIR, we conduct experiments on 2 HumanoidBench locomotion tasks without dexterous hands and 4 locomotion tasks with dexterous hands. Episode return results in Table 1 show that CIR consistently beats SimBa, sometimes by a significant margin. This further verifies the advantages of using CIR.

6.3 ABLATION STUDY

In this part, we conduct a detailed ablation study of CIR. We first adopt 7 DMC medium tasks and 7 DMC hard tasks for experiments, and consider (i) **NoTanh**, where we discard the Tanh function in CIR; (ii) **NoLN**, a variant of CIR without layer normalization; (iii) **CDQ**, which utilizes CDQ instead of the convex Q-learning; (iv) **UTD**, which replaces SMR with UTD in CIR (UTD = 2). We summarize the results in Figure 5 (left), where we report the percent CIR performance (% CIR performance) of these variants. If the percent CIR performance exceeds 100, it indicates that the variant outperforms CIR, and underperforms CIR if it is smaller than 100. We further use 20 DMC easy & medium tasks for experiments and consider (v) **Sigmoid**, (vi) **Softmax**, (vii) **LayerNorm**, that replace Tanh with sigmoid, softmax, and layer normalization, respectively; (viii) **NoSC**, which removes the skip connection module in CIR. The results are presented in Figure 5 (right).

On the critic network architecture. It turns out that eliminating either the Tanh function or layer normalization decreases the performance of CIR, especially on complex DMC hard tasks. The Tanh function is responsible for initial representation constraint, while layer normalization ensures that the representations in downstream layers are stabilized. Layer normalization also serves as a regularization term (as required in Theorem 4.5). Both of them are vital for CIR. Also, either removing the skip connection module or replacing the Tanh function with sigmoid, softmax, or layer normalization can incur performance drop. These verify our design choice on network components.

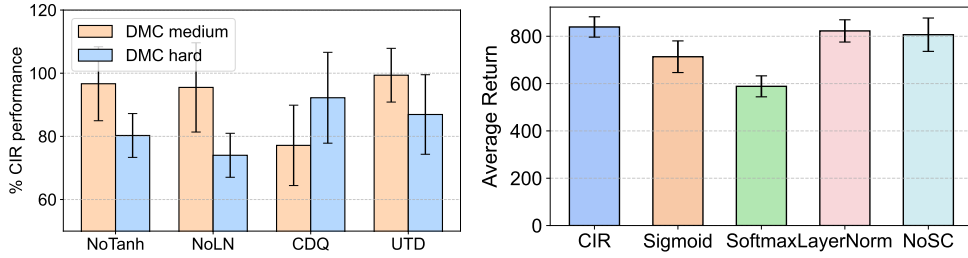


Figure 5: **Left:** Ablation study on network components and algorithmic components in CIR. **Right:** Ablation study on Tanh and skip connection module in CIR. SC denotes skip connection.

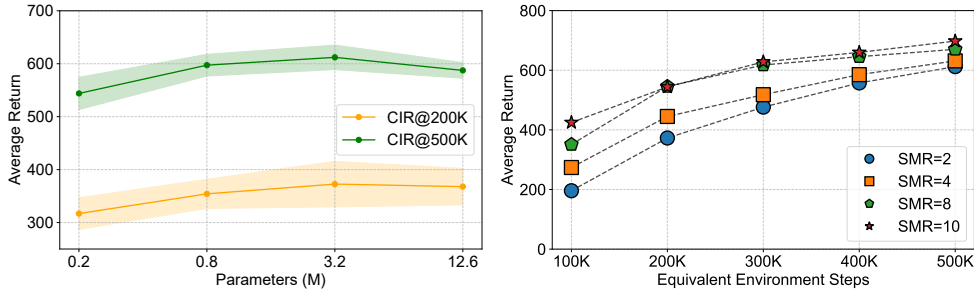


Figure 6: **Scaling results of CIR.** We report the scaling results on network capacity (**left**) and the SMR ratio (**right**). We use the aggregated average return for performance comparison.

On algorithmic components. The results show that adopting CDQ for value estimate causes significant performance decrease. This validates our claim in Section 5.3 and stresses the necessity of convex Q-learning. We observe that UTD achieves similar performance as CIR on medium tasks but its performance on hard tasks is worse than CIR, demonstrating the superiority of SMR over UTD.

6.4 SCALING RESULTS

We now investigate the scaling capability of CIR, and adopt 6 DMC medium tasks, 3 DMC hard tasks for experiments. Since medium tasks are run for 500K steps while hard tasks are run for 1M steps, we define *equivalent environment step* k that aligns the actual environment step of medium and hard tasks. Reporting average returns under equivalent environment step k means that we aggregate returns of medium tasks at environment step k and hard tasks at environment step $2k$. We denote CIR@ k as the (aggregated) return of CIR at k -th step in medium tasks and $2k$ -th step in hard tasks. For example, CIR@200K means the aggregated return of DMC medium tasks at 200K steps and hard tasks at 400K steps. The empirical results are outlined in Figure 6.

Scaling the network size. We scale the width of the CIR critic networks and the actor network by varying the size of the hidden dimension in $\{128, 256, 512, 1024\}$. The results in Figure 6 (left) illustrate that CIR generally benefits from scaling the network capacity across different equivalent environment steps. The performance of CIR grows slowly upon reaching a certain amount of parameters, which matches the reported scaling results in (Nauman et al., 2024; Lee et al., 2025a).

Scaling the SMR ratio. We then investigate whether CIR can benefit from scaling computation time by measuring the performance of CIR across different SMR ratios (from 2 to 10). Figure 6 (right) demonstrates that CIR consistently enjoys performance improvement by increasing the SMR ratio under various equivalent environment steps, especially at the initial training stage.

7 CONCLUSION AND FUTURE OPPORTUNITIES

Our key contribution in this work is the CIR framework, which aims at enhancing the sample efficiency from the perspective of initial representation constraint. CIR introduces three novel components, (i) restricting initial representations by leveraging the Tanh function, layer normalization, and AvgRNorm; (ii) the skip connection technique that offers a linear pathway from the low-level

features to deep abstract representation; (iii) the convex Q-learning approach that returns optimistic and flexible value estimate. We provide theoretical guarantees for our method under linear function approximation. Moreover, empirical evaluations on the DMC suite, HumanoidBench and ODRL tasks show that CIR exhibits competitive or even better performance against recent strong baselines.

Opportunities. We believe that this work offers a valuable attempt at improving sample efficiency by constraining initial representations, offering opportunities for proposing better representation stabilization methods (e.g., combining various normalization tricks) or designing better architectures.

REPRODUCIBILITY STATEMENT

We have made efforts to ensure that our work is reproducible. We provide the source code of our algorithm in the supplementary materials. Additionally, we provide the detailed hyperparameter setup for CIR in Appendix D, and the details on benchmark environments in Appendix C.

REFERENCES

Rishabh Agarwal, Max Schwarzer, Pablo Samuel Castro, Aaron C Courville, and Marc Bellemare. Deep reinforcement learning at the edge of the statistical precipice. *Advances in neural information processing systems*, 34:29304–29320, 2021.

Marcin Andrychowicz, Filip Wolski, Alex Ray, Jonas Schneider, Rachel Fong, Peter Welinder, Bob McGrew, Josh Tobin, OpenAI Pieter Abbeel, and Wojciech Zaremba. Hindsight experience replay. *Advances in neural information processing systems*, 30, 2017.

Marcin Andrychowicz, Anton Raichuk, Piotr Sta’nczyk, Manu Orsini, Sertan Girgin, Raphaël Marinier, L’eonard Hussenot, Matthieu Geist, Olivier Pietquin, Marcin Michalski, Sylvain Gelly, and Olivier Bachem. What matters in on-policy reinforcement learning? a large-scale empirical study. *ArXiv*, abs/2006.05990, 2020.

John Asmuth, Lihong Li, Michael L Littman, Ali Nouri, and David Wingate. A bayesian sampling approach to exploration in reinforcement learning. *arXiv preprint arXiv:1205.2664*, 2012.

Jimmy Ba, Jamie Ryan Kiros, and Geoffrey E. Hinton. Layer normalization. *ArXiv*, abs/1607.06450, 2016.

Maximilian Beck, Korbinian Poppel, Markus Spanring, Andreas Auer, Oleksandra Prudnikova, Michael K Kopp, Günter Klambauer, Johannes Brandstetter, and Sepp Hochreiter. xlstm: Extended long short-term memory. *ArXiv*, abs/2405.04517, 2024.

Marc G Bellemare, Will Dabney, and Rémi Munos. A distributional perspective on reinforcement learning. In *International conference on machine learning*, pp. 449–458. PMLR, 2017.

Jalaj Bhandari, Daniel Russo, and Raghav Singal. A finite time analysis of temporal difference learning with linear function approximation. In *Conference on learning theory*, pp. 1691–1692. PMLR, 2018.

Aditya Bhatt, Daniel Palenicek, Boris Belousov, Max Argus, Artemij Amiranashvili, Thomas Brox, and Jan Peters. Crossq: Batch normalization in deep reinforcement learning for greater sample efficiency and simplicity. In *The Twelfth International Conference on Learning Representations*, 2024. URL <https://openreview.net/forum?id=PczQtTsTIX>.

Johan Bjorck, Carla P. Gomes, and Kilian Q. Weinberger. Towards deeper deep reinforcement learning. In *Neural Information Processing Systems*, 2021.

Jacob Buckman, Danijar Hafner, George Tucker, Eugene Brevdo, and Honglak Lee. Sample-efficient reinforcement learning with stochastic ensemble value expansion. *Advances in neural information processing systems*, 31, 2018.

Yuri Burda, Harrison Edwards, Amos Storkey, and Oleg Klimov. Exploration by random network distillation. *arXiv preprint arXiv:1810.12894*, 2018.

Xinyue Chen, Che Wang, Zijian Zhou, and Keith W. Ross. Randomized ensembled double q-learning: Learning fast without a model. In *International Conference on Learning Representations*, 2021. URL <https://openreview.net/forum?id=AY8zfZm0tDd>.

Kamil Ciosek, Quan Vuong, Robert Loftin, and Katja Hofmann. Better exploration with optimistic actor critic. *Advances in Neural Information Processing Systems*, 32, 2019.

Tim De Bruin, Jens Kober, Karl Tuyls, and Robert Babuška. Integrating state representation learning into deep reinforcement learning. *IEEE Robotics and Automation Letters*, 3(3):1394–1401, 2018.

Jacob Devlin, Ming-Wei Chang, Kenton Lee, and Kristina Toutanova. Bert: Pre-training of deep bidirectional transformers for language understanding. In *North American Chapter of the Association for Computational Linguistics*, 2019.

Pierluca D’Oro and Wojciech Jaśkowski. How to learn a useful critic? model-based action-gradient-estimator policy optimization. *Advances in neural information processing systems*, 33:313–324, 2020.

Pierluca D’Oro, Max Schwarzer, Evgenii Nikishin, Pierre-Luc Bacon, Marc G Bellemare, and Aaron Courville. Sample-efficient reinforcement learning by breaking the replay ratio barrier. In *The Eleventh International Conference on Learning Representations*, 2023. URL <https://openreview.net/forum?id=OpC-9aBBVJe>.

Simon Shaolei Du, Sham M. Kakade, Ruosong Wang, and Lin F. Yang. Is a good representation sufficient for sample efficient reinforcement learning? *ArXiv*, abs/1910.03016, 2019.

Mohamed Elsayed, Gautham Vasan, and A. Rupam Mahmood. Streaming deep reinforcement learning finally works. *ArXiv*, abs/2410.14606, 2024.

Benjamin Eysenbach, Shreyas Chaudhari, Swapnil Asawa, Sergey Levine, and Ruslan Salakhutdinov. Off-dynamics reinforcement learning: Training for transfer with domain classifiers. In *International Conference on Learning Representations*, 2021. URL <https://openreview.net/forum?id=eqBwg3AcIAK>.

Benjamin Eysenbach, Matthieu Geist, Sergey Levine, and Ruslan Salakhutdinov. A connection between one-step regularization and critic regularization in reinforcement learning. *arXiv preprint arXiv:2307.12968*, 2023.

Jesse Farebrother, Marlos C. Machado, and Michael H. Bowling. Generalization and regularization in dqn. *ArXiv*, abs/1810.00123, 2018.

Scott Fujimoto, Herke Hoof, and David Meger. Addressing function approximation error in actor-critic methods. In *International Conference on Machine Learning*, pp. 1587–1596. PMLR, 2018.

Scott Fujimoto, David Meger, and Doina Precup. An equivalence between loss functions and non-uniform sampling in experience replay. *Advances in neural information processing systems*, 33: 14219–14230, 2020.

Scott Fujimoto, Wei-Di Chang, Edward J. Smith, Shixiang Shane Gu, Doina Precup, and David Meger. For SALE: State-action representation learning for deep reinforcement learning. In *Thirty-seventh Conference on Neural Information Processing Systems*, 2023. URL <https://openreview.net/forum?id=xZvGrzRq17>.

Scott Fujimoto, Pierluca D’Oro, Amy Zhang, Yuandong Tian, and Michael Rabbat. Towards general-purpose model-free reinforcement learning. In *The Thirteenth International Conference on Learning Representations*, 2025. URL <https://openreview.net/forum?id=R1hIXdST22>.

Matteo Gallici, Mattie Fellows, Benjamin Ellis, Bartomeu Pou, Ivan Masmitja, Jakob Nicolaus Foerster, and Mario Martin. Simplifying deep temporal difference learning. In *The Thirteenth International Conference on Learning Representations*, 2025. URL <https://openreview.net/forum?id=7IzeL0kflu>.

Florin Gogianu, Tudor Berariu, Mihaela Rosca, Claudia Clopath, Lucian Buşoniu, and Razvan Pascanu. Spectral normalisation for deep reinforcement learning: an optimisation perspective. In *International Conference on Machine Learning*, 2021.

Ian Goodfellow, Yoshua Bengio, Aaron Courville, and Yoshua Bengio. *Deep learning*. MIT press Cambridge, 2016.

Ian J. Goodfellow, Jean Pouget-Abadie, Mehdi Mirza, Bing Xu, David Warde-Farley, Sherjil Ozair, Aaron C. Courville, and Yoshua Bengio. Generative adversarial networks. 2023 14th International Conference on Computing Communication and Networking Technologies (ICCCNT), pp. 1–7, 2021.

Tuomas Haarnoja, Aurick Zhou, Kristian Hartikainen, George Tucker, Sehoon Ha, Jie Tan, Vikash Kumar, Henry Zhu, Abhishek Gupta, Pieter Abbeel, et al. Soft actor-critic algorithms and applications. *arXiv preprint arXiv:1812.05905*, 2018.

Danijar Hafner, Jurgis Pasukonis, Jimmy Ba, and Timothy Lillicrap. Mastering diverse domains through world models. *arXiv preprint arXiv:2301.04104*, 2023.

Nicklas Hansen, Hao Su, and Xiaolong Wang. TD-MPC2: Scalable, robust world models for continuous control. In *The Twelfth International Conference on Learning Representations*, 2024. URL <https://openreview.net/forum?id=Oxh5CstDJU>.

Nicklas A Hansen, Hao Su, and Xiaolong Wang. Temporal difference learning for model predictive control. In *International Conference on Machine Learning*, pp. 8387–8406. PMLR, 2022.

Kaiming He, X. Zhang, Shaoqing Ren, and Jian Sun. Deep residual learning for image recognition. *2016 IEEE Conference on Computer Vision and Pattern Recognition (CVPR)*, pp. 770–778, 2015.

Takuya Hiraoka, Takahisa Imagawa, Taisei Hashimoto, Takashi Onishi, and Yoshimasa Tsuruoka. Dropout q-functions for doubly efficient reinforcement learning. *ArXiv*, abs/2110.02034, 2021.

Jonathan Ho, Ajay Jain, and P. Abbeel. Denoising diffusion probabilistic models. *ArXiv*, abs/2006.11239, 2020.

Michael Janner, Justin Fu, Marvin Zhang, and Sergey Levine. When to trust your model: Model-based policy optimization. *Advances in neural information processing systems*, 32, 2019.

Yuhua Jiang, Qihan Liu, Yiqin Yang, Xiaoteng Ma, Dianyu Zhong, Hao Hu, Jun Yang, Bin Liang, Bo XU, Chongjie Zhang, and Qianchuan Zhao. Episodic novelty through temporal distance. In *The Thirteenth International Conference on Learning Representations*, 2025. URL <https://openreview.net/forum?id=I7DeajDEX7>.

Chi Jin, Zhuoran Yang, Zhaoran Wang, and Michael I Jordan. Provably efficient reinforcement learning with linear function approximation. In *Conference on learning theory*, pp. 2137–2143. PMLR, 2020.

Hamed Karimi, Julie Nutini, and Mark Schmidt. Linear convergence of gradient and proximal-gradient methods under the polyak-łojasiewicz condition. In *Joint European conference on machine learning and knowledge discovery in databases*, pp. 795–811. Springer, 2016.

Diederik P Kingma and Jimmy Ba. Adam: A method for stochastic optimization. *arXiv preprint arXiv:1412.6980*, 2014.

Ilya Kostrikov, Jonathan Tompson, Rob Fergus, and Ofir Nachum. Offline reinforcement learning with fisher divergence critic regularization. In *International Conference on Machine Learning*, 2021.

Arsenii Kuznetsov, Pavel Shvchikov, Alexander Grishin, and Dmitry Vetrov. Controlling overestimation bias with truncated mixture of continuous distributional quantile critics. In *International Conference on Machine Learning*, pp. 5556–5566. PMLR, 2020.

Pawel Ladosz, Lilian Weng, Minwoo Kim, and Hyondong Oh. Exploration in deep reinforcement learning: A survey. *Information Fusion*, 85:1–22, 2022.

Michael Laskin, Aravind Srinivas, and Pieter Abbeel. Curl: Contrastive unsupervised representations for reinforcement learning. In *International conference on machine learning*, pp. 5639–5650. PMLR, 2020.

Hojoon Lee, Dongyoong Hwang, Donghu Kim, Hyunseung Kim, Jun Jet Tai, Kaushik Subramanian, Peter R. Wurman, Jaegul Choo, Peter Stone, and Takuma Seno. Simba: Simplicity bias for scaling up parameters in deep reinforcement learning. In *The Thirteenth International Conference on Learning Representations*, 2025a. URL <https://openreview.net/forum?id=jXLiDKsuDo>.

Hojoon Lee, Youngdo Lee, Takuma Seno, Donghu Kim, Peter Stone, and Jaegul Choo. Hyperspherical normalization for scalable deep reinforcement learning. *ArXiv*, abs/2502.15280, 2025b.

Felix Leibfried and Jordi Grau-Moya. Mutual-information regularization in markov decision processes and actor-critic learning. In *Conference on Robot Learning*, 2019.

Xihui Li, Zhongjian Qiao, Aicheng Gong, Jiafei Lyu, Chenghui Yu, Jiangpeng Yan, and Xiu Li. Prag: Periodic regularized action gradient for efficient continuous control. In *Pacific Rim International Conference on Artificial Intelligence*, pp. 106–119. Springer, 2022.

Jiafei Lyu, Xiaoteng Ma, Jiangpeng Yan, and Xiu Li. Efficient continuous control with double actors and regularized critics. In *Proceedings of the AAAI Conference on Artificial Intelligence*, pp. 7655–7663, 2022.

Jiafei Lyu, Yu Yang, Jiangpeng Yan, and Xiu Li. Value activation for bias alleviation: Generalized-activated deep double deterministic policy gradients. *Neurocomputing*, 518:70–81, 2023.

Jiafei Lyu, Chenjia Bai, Jing-Wen Yang, Zongqing Lu, and Xiu Li. Cross-domain policy adaptation by capturing representation mismatch. In *Forty-first International Conference on Machine Learning*, 2024a. URL <https://openreview.net/forum?id=3uPSQmjXzd>.

Jiafei Lyu, Le Wan, Xiu Li, and Zongqing Lu. Off-policy rl algorithms can be sample-efficient for continuous control via sample multiple reuse. *Information Sciences*, 666:120371, 2024b.

Jiafei Lyu, Kang Xu, Jiacheng Xu, Mengbei Yan, Jing-Wen Yang, Zongzhang Zhang, Chenjia Bai, Zongqing Lu, and Xiu Li. ODRL: A benchmark for off-dynamics reinforcement learning. In *The Thirty-eighth Conference on Neural Information Processing Systems Datasets and Benchmarks Track*, 2024c. URL <https://openreview.net/forum?id=ap4x1kArGy>.

Stephen Merity, Nitish Shirish Keskar, and Richard Socher. Regularizing and optimizing lstm language models. *arXiv preprint arXiv:1708.02182*, 2017.

Fausto Milletari, Nassir Navab, and Seyed-Ahmad Ahmadi. V-net: Fully convolutional neural networks for volumetric medical image segmentation. In *2016 fourth international conference on 3D vision (3DV)*, pp. 565–571. Ieee, 2016.

Ted Moskovitz, Jack Parker-Holder, Aldo Pacchiano, Michael Arbel, and Michael Jordan. Tactile optimism and pessimism for deep reinforcement learning. *Advances in Neural Information Processing Systems*, 34:12849–12863, 2021.

Michał Nauman, Mateusz Ostaszewski, Krzysztof Jankowski, Piotr Miłoś, and Marek Cygan. Bigger, regularized, optimistic: scaling for compute and sample efficient continuous control. In *The Thirty-eighth Annual Conference on Neural Information Processing Systems*, 2024. URL <https://openreview.net/forum?id=fu0xdh4aEJ>.

Yurii Nesterov. *Introductory lectures on convex optimization: A basic course*, volume 87. Springer Science & Business Media, 2013.

Evgenii Nikishin, Max Schwarzer, Pierluca D’Oro, Pierre-Luc Bacon, and Aaron C. Courville. The primacy bias in deep reinforcement learning. In *International Conference on Machine Learning*, 2022.

Kei Ota, Tomoaki Oiki, Devesh Jha, Toshisada Mariyama, and Daniel Nikovski. Can increasing input dimensionality improve deep reinforcement learning? In *International conference on machine learning*, pp. 7424–7433. PMLR, 2020.

Daniel Palenicek, Florian Vogt, and Jan Peters. Scaling off-policy reinforcement learning with batch and weight normalization. *ArXiv*, abs/2502.07523, 2025.

Ling Pan, Qingpeng Cai, and Longbo Huang. Softmax deep double deterministic policy gradients. *Advances in neural information processing systems*, 33:11767–11777, 2020.

Simone Parisi, Voot Tangkaratt, Jan Peters, and Mohammad Emamiyaz Khan. Td-regularized actor-critic methods. *Machine Learning*, 108:1467 – 1501, 2018.

Zhongjian Qiao, Jiafei Lyu, and Xiu Li. Mind the model, not the agent: The primacy bias in model-based rl. In *European Conference on Artificial Intelligence*, 2024.

Carlo Romeo, Girolamo Macaluso, Alessandro Sestini, and Andrew D Bagdanov. Speq: Stabilization phases for efficient q-learning in high update-to-data ratio reinforcement learning. *arXiv preprint arXiv:2501.08669*, 2025.

Olaf Ronneberger, Philipp Fischer, and Thomas Brox. U-net: Convolutional networks for biomedical image segmentation. In *Medical image computing and computer-assisted intervention-MICCAI 2015: 18th international conference, Munich, Germany, October 5-9, 2015, proceedings, part III 18*, pp. 234–241. Springer, 2015.

Tom Schaul, John Quan, Ioannis Antonoglou, and David Silver. Prioritized experience replay. *arXiv preprint arXiv:1511.05952*, 2015.

Max Schwarzer, Johan Obando-Ceron, Aaron C. Courville, Marc G. Bellemare, Rishabh Agarwal, and Pablo Samuel Castro. Bigger, better, faster: Human-level atari with human-level efficiency. In *International Conference on Machine Learning*, 2023.

Carmelo Sferrazza, Dun-Ming Huang, Xingyu Lin, Youngwoon Lee, and Pieter Abbeel. Humanoid-bench: Simulated humanoid benchmark for whole-body locomotion and manipulation. *arXiv preprint arXiv:2403.10506*, 2024.

Lin Shao, Yifan You, Mengyuan Yan, Shenli Yuan, Qingyun Sun, and Jeannette Bohg. Grac: Self-guided and self-regularized actor-critic. In *Conference on Robot Learning*, pp. 267–276. PMLR, 2022.

Ghada Sokar, Rishabh Agarwal, Pablo Samuel Castro, and Utku Evci. The dormant neuron phenomenon in deep reinforcement learning. In *International Conference on Machine Learning*, 2023.

Nitish Srivastava, Geoffrey E. Hinton, Alex Krizhevsky, Ilya Sutskever, and Ruslan Salakhutdinov. Dropout: a simple way to prevent neural networks from overfitting. *Journal of Machine Learning Research*, 15:1929–1958, 2014.

Susanne Still and Doina Precup. An information-theoretic approach to curiosity-driven reinforcement learning. *Theory in Biosciences*, 131(3):139–148, 2012.

Kefan Su and Zongqing Lu. Divergence-regularized multi-agent actor-critic. In *International Conference on Machine Learning*, 2021.

Meng Tang, Federico Perazzi, Abdelaziz Djelouah, Ismail Ben Ayed, Christopher Schroers, and Yuri Boykov. On regularized losses for weakly-supervised cnn segmentation. In *Proceedings of the European conference on computer vision (ECCV)*, pp. 507–522, 2018.

Sasha Targ, Diogo Almeida, and Kevin Lyman. Resnet in resnet: Generalizing residual architectures. *ArXiv*, abs/1603.08029, 2016.

Yuval Tassa, Yotam Doron, Alistair Muldal, Tom Erez, Yazhe Li, Diego de Las Casas, David Budden, Abbas Abdolmaleki, Josh Merel, Andrew Lefrancq, et al. Deepmind control suite. *arXiv preprint arXiv:1801.00690*, 2018.

John Tsitsiklis and Benjamin Van Roy. Analysis of temporal-difference learning with function approximation. *Advances in neural information processing systems*, 9, 1996.

Hado Van Hasselt, Arthur Guez, and David Silver. Deep reinforcement learning with double q-learning. In *Proceedings of the AAAI conference on artificial intelligence*, 2016.

Ashish Vaswani, Noam M. Shazeer, Niki Parmar, Jakob Uszkoreit, Llion Jones, Aidan N. Gomez, Łukasz Kaiser, and Illia Polosukhin. Attention is all you need. In *Neural Information Processing Systems*, 2017.

Claas A Voelcker, Marcel Hussing, Eric Eaton, Amir massoud Farahmand, and Igor Gilitschenski. MAD-TD: Model-augmented data stabilizes high update ratio RL. In *The Thirteenth International Conference on Learning Representations*, 2025. URL <https://openreview.net/forum?id=6RtRsg8ZV1>.

Xin Wang, Yi Qin, Yi Wang, Sheng Xiang, and Haizhou Chen. Reltanh: An activation function with vanishing gradient resistance for sae-based dnns and its application to rotating machinery fault diagnosis. *Neurocomputing*, 363:88–98, 2019.

Yue Wu, Shuangfei Zhai, Nitish Srivastava, Joshua M. Susskind, Jian Zhang, Ruslan Salakhutdinov, and Hanlin Goh. Uncertainty weighted actor-critic for offline reinforcement learning. In *International Conference on Machine Learning*, 2021.

Lingxi Xie, Jingdong Wang, Zhen Wei, Meng Wang, and Qi Tian. Disturblabel: Regularizing cnn on the loss layer. In *Proceedings of the IEEE conference on computer vision and pattern recognition*, pp. 4753–4762, 2016.

Ji Xin, Raphael Tang, Yaoliang Yu, and Jimmy Lin. The art of abstention: Selective prediction and error regularization for natural language processing. In *Proceedings of the 59th Annual Meeting of the Association for Computational Linguistics and the 11th International Joint Conference on Natural Language Processing (Volume 1: Long Papers)*, pp. 1040–1051, 2021.

Chunyan Xu, Canyi Lu, Xiaodan Liang, Junbin Gao, Wei Zheng, Tianjiang Wang, and Shuicheng Yan. Multi-loss regularized deep neural network. *IEEE Transactions on Circuits and Systems for Video Technology*, 26(12):2273–2283, 2015.

Guowei Xu, Ruijie Zheng, Yongyuan Liang, Xiyao Wang, Zhecheng Yuan, Tianying Ji, Yu Luo, Xiaoyu Liu, Jiaxin Yuan, Pu Hua, Shuzhen Li, Yanjie Ze, Hal Daumé III, Furong Huang, and Huazhe Xu. Drm: Mastering visual reinforcement learning through dormant ratio minimization. In *The Twelfth International Conference on Learning Representations*, 2024. URL <https://openreview.net/forum?id=MSe8YFbhUE>.

Mengbei Yan, Jiafei Lyu, and Xiu Li. Enhancing visual reinforcement learning with state–action representation. *Knowledge-Based Systems*, 304:112487, 2024.

Kai Yang, Jian Tao, Jiafei Lyu, and Xiu Li. Exploration and anti-exploration with distributional random network distillation. In *Forty-first International Conference on Machine Learning*, 2024. URL <https://openreview.net/forum?id=rIrpzmqRBk>.

Yang Yu. Towards sample efficient reinforcement learning. In *IJCAI*, pp. 5739–5743, 2018.

Shangtong Zhang, Remi Tachet Des Combes, and Romain Laroche. On the convergence of sarsa with linear function approximation. In *International Conference on Machine Learning*, pp. 41613–41646. PMLR, 2023.

Shaofeng Zou, Tengyu Xu, and Yingbin Liang. Finite-sample analysis for sarsa with linear function approximation. *Advances in neural information processing systems*, 32, 2019.

A MISSING PROOFS

In this section, we provide missing proofs for theorems in the main text. The convergent behavior of TD learning is studied in prior works like (Gallici et al., 2025), but we focus on convergent behaviors of TD learning under Tanh activation. For better readability, we restate all theorems.

A.1 PROOF OF THEOREM 4.2

Theorem A.1 (Linear Independence). *Suppose that $W = c \cdot I$, where $c \in \mathbb{R}$ is a sufficient small positive number, I is the identity matrix, then if basis functions $\{\phi_1, \dots, \phi_S\}$ are linearly independent, then the transformed basis functions $\{\tanh(W\phi_1), \dots, \tanh(W\phi_S)\}$ are also linearly independent.*

Proof. Since we set $W = c \cdot I$, we have $\tanh(W\phi_j) = \tanh(c \cdot \phi_j), \forall j \in \{1, 2, \dots, S\}$. Based on the assumption that the basis functions $\{\phi_1, \dots, \phi_S\}$ are linearly independent, the only solution to the equation

$$\sum_{i=1}^S a_i \phi_i = 0 \quad (11)$$

is $a_1 = a_2 = \dots = a_S = 0$. When c is sufficiently small, $c \cdot \phi_i$ is also sufficiently small, $\forall i \in \{1, 2, \dots, S\}$. By using Taylor expansion of $\tanh(x)$ around $x = 0$, we have

$$\tanh(x) = x - \frac{x^3}{3} + \frac{2x^5}{15} - \dots = x + \mathcal{O}(x^3). \quad (12)$$

Thus, for $c \cdot \phi_i \approx \mathbf{0}$ where $\mathbf{0}$ is d -dimensional zero matrix, we have

$$\tanh(c \cdot \phi_i) = c \cdot \phi_i + \mathcal{O}(c^3 \|\phi_i\|^3). \quad (13)$$

Suppose there exists a non-zero coefficient vector $\mathbf{a} = (a_1, a_2, \dots, a_S)$ such that

$$\sum_{i=1}^S a_i \tanh(c \cdot \phi_i) = 0. \quad (14)$$

Substituting the Taylor expansion, we get

$$\sum_{i=1}^S a_i (c \cdot \phi_i + \mathcal{O}(c^3 \|\phi_i\|^3)) = 0, \quad (15)$$

which simplifies to

$$\sum_{i=1}^S a_i \phi_i + \mathcal{O}(c^2) = 0. \quad (16)$$

As $c \rightarrow 0$, the remainder term $\mathcal{O}(c^2) \rightarrow 0$. By the continuity of linear combinations, we obtain

$$\sum_{i=1}^S a_i \phi_i = 0, \quad (17)$$

which contradicts the linear independence of $\{\phi_i\}$. Thus, no such non-zero vector \mathbf{a} can exist for sufficiently small c . This indicates that the transformed basis functions $\{\tanh(W\phi_1), \dots, \tanh(W\phi_S)\}$ are also linearly independent. \square

A.2 PROOF OF THEOREM 4.3

Theorem A.2 (Variance Reduction). *Given any state s , we assume the feature $\phi(s)$ follows a distribution with $\mathbb{E}[\phi(s)] = 0$. Consider per-transition least square TD (LSTD) objective $\mathcal{L} = \frac{1}{2}[(r + \gamma V(s'; \theta) - V(s; \theta))^2]$, then if $V(s; \theta) = \phi(s)^\top \theta$, the variance of the semi-gradient term satisfies:*

$$\|\text{Var}(\nabla_\theta \mathcal{L})\| \leq (r_{\max} + (1 + \gamma)\|\theta\|\Lambda)^2 \cdot \|\phi(s)\|^2, \quad (18)$$

where $\Lambda = \max\{\|\phi(s)\|, \|\phi(s')\|\}$. While if $V(s; \theta) = \tanh(W\phi(s))^\top \theta$, we have

$$\|\text{Var}(\nabla_\theta \mathcal{L})\| \leq (r_{\max} + (1 + \gamma)\|\theta\|\lambda_W\Lambda)^2 \cdot \|\tanh(W\phi(s))\|^2, \quad (19)$$

where λ_W is the maximum eigenvalue of W .

Proof. Given the objective function

$$\mathcal{L} = \frac{1}{2}[(r + \gamma V(s'; \theta) - V(s; \theta))^2], \quad (20)$$

it is easy to find its semi-gradient term,

$$\nabla \mathcal{L} = (r + \gamma V(s'; \theta) - V(s; \theta))\nabla V(s; \theta). \quad (21)$$

If $V(s; \theta) = \phi(s)^\top \theta$, we have

$$\nabla_\theta \mathcal{L} = (r + \gamma \phi(s')^\top \theta - \phi(s)^\top \theta)\phi(s). \quad (22)$$

Recall that $\text{Var}(X) = \mathbb{E}[X^2] - (\mathbb{E}X)^2$, we notice that $\phi(s)^\top \theta, \phi(s')^\top \theta$ are scalar values, by using the assumption, it is easy to find that

$$\mathbb{E}[\nabla_\theta \mathcal{L}] = \mathbb{E}[(r + \gamma \phi(s')^\top \theta - \phi(s)^\top \theta)\phi(s)] = (r + \gamma \phi(s')^\top \theta - \phi(s)^\top \theta)\mathbb{E}[\phi(s)] = 0. \quad (23)$$

Therefore, we have

$$\text{Var}(\nabla_\theta \mathcal{L}) = \mathbb{E}[\nabla_\theta \mathcal{L}]^2 = [r + \gamma \phi(s')^\top \theta - \phi(s)^\top \theta]^2 \mathbb{E}[\phi(s)\phi(s)^\top]. \quad (24)$$

Then,

$$\|\text{Var}(\nabla_\theta \mathcal{L})\| = \|[r + \gamma \phi(s')^\top \theta - \phi(s)^\top \theta]^2 \mathbb{E}[\phi(s)\phi(s)^\top]\| \quad (25)$$

$$\leq (r_{\max} + \gamma \|\phi(s')\| \|\theta\| + \|\phi(s)\| \|\theta\|)^2 \|\phi(s)\|^2 \quad (26)$$

$$\leq (r_{\max} + (1 + \gamma)\|\theta\|\Lambda)^2 \|\phi(s)\|^2, \quad (27)$$

where $\Lambda = \max\{\|\phi(s)\|, \|\phi(s')\|\}$. While if $V(s; \theta) = \tanh(W\phi(s))^\top \theta$, where W is a positive definite diagonal matrix, the semi-gradient gives

$$\nabla_\theta \mathcal{L} = \underbrace{(r + \gamma \tanh(W\phi(s'))^\top \theta - \tanh(W\phi(s))^\top \theta)}_{:=\delta} \tanh(W\phi(s)). \quad (28)$$

We first bound $\mathbb{E}[\nabla_\theta \mathcal{L}]^2$ term,

$$\mathbb{E}[\nabla_\theta \mathcal{L}]^2 = \|[r + \gamma \tanh(W\phi(s'))^\top \theta - \tanh(W\phi(s))^\top \theta]^2 \mathbb{E}[\tanh(W\phi(s))\tanh(W\phi(s))^\top]\| \quad (29)$$

$$\leq (r_{\max} + \gamma \|\tanh(W\phi(s'))\| \|\theta\| + \|\tanh(W\phi(s))\| \|\theta\|)^2 \cdot \|\tanh(W\phi(s))\|^2 \quad (30)$$

$$= (r_{\max} + (1 + \gamma)\|\theta\|\lambda_W\Lambda)^2 \cdot \|\tanh(W\phi(s))\|^2, \quad (31)$$

where the last inequality holds due to $\|\tanh(W\phi(s))\| \leq \|W\phi(s)\| \leq \lambda_W \|\phi(s)\| \leq \lambda_W \Lambda$.

Unfortunately, $\mathbb{E}[\phi(s)] = 0$ does not necessarily guarantee that $\mathbb{E}[\tanh(W\phi(s))^\top \theta] = 0$. Nevertheless, we have $\|\tanh(W\phi(s))\| \leq \sqrt{d}$ since $|\tanh(x)| \leq 1$. We then have the variance term,

$$\|\text{Var}(\nabla_\theta \mathcal{L})\| = \mathbb{E}[\nabla_\theta \mathcal{L}]^2 - (\mathbb{E}[\nabla_\theta \mathcal{L}])^2 \quad (32)$$

$$\leq \mathbb{E}[\nabla_\theta \mathcal{L}]^2 = (r_{\max} + (1 + \gamma)\|\theta\|\lambda_W\Lambda)^2 \cdot \|\tanh(W\phi(s))\|^2. \quad (33)$$

These conclude the proof. \square

A.3 PROOF OF THEOREM 4.4

Theorem A.3 (Convergence under TD(0)). *Consider the TD(0) update rule for the value function $V(s; \theta) = \tanh(W\phi(s))^\top \theta$. Suppose we project the parameters θ onto bounded sets $\Theta = \{\theta \mid \|\theta\|_2 \leq C_\theta\}$ after each update. If the step sizes satisfy $\sum \alpha_t = \infty$, $\sum \alpha_t^2 < \infty$, then the projected TD(0) algorithm converges almost surely to a fixed point θ^* .*

Proof. Denote $\tilde{\phi}(s) = \tanh(W\phi(s))$, then the value function becomes $V(s; \theta) = \tilde{\phi}^\top \theta$, and the new features $\tilde{\phi}(s)$ satisfy $\|\tilde{\phi}(s)\| = \|\tanh(W\phi(s))\| \leq \sqrt{d} < \infty$. Therefore, the problem degenerates into the convergence of TD(0) under the formulation $V(s; \theta) = \tilde{\phi}^\top \theta$, which is a well-known result based on Theorem 1 in (Tsitsiklis & Van Roy, 1996). The resulting fixed point θ^* is the fixed point of the projected Bellman equation,

$$\tanh(W\phi(s))^\top \theta = \Pi_\nu \mathcal{T}(\tanh(W\phi(s))^\top \theta), \quad (34)$$

where $\Pi_\nu(x) = \arg \min_{z \in \tanh(W\phi(s))^\top \theta} \|z - x\|_\nu^2$, \mathcal{T} is the Bellman operator, ν is the stationary distribution of the Markov chain. \square

A.4 PROOF OF THEOREM 4.5

Theorem A.4 (Global Convergence under Regularization). *Given the regularized loss $\mathcal{L}(\theta) = \mathbb{E} \left[(r + \gamma \tanh(W\phi(s'))^\top \theta - \tanh(W\phi(s))^\top \theta)^2 \right] + \lambda_\theta \|\theta\|_2^2$, assume that (a) the step size α is a constant; (b) the gradient of the loss $\mathcal{L}(\theta)$ is β -smooth, i.e., $\|\nabla \mathcal{L}(\theta_1) - \nabla \mathcal{L}(\theta_2)\| \leq \beta \|\theta_1 - \theta_2\|$; (c) the regularization parameter satisfies $0 < \lambda_\theta < \frac{\beta}{2}$. Then, gradient descent with step size $\alpha \leq 1/\beta$ converges linearly to a unique global minimum θ^* .*

Proof. The loss function combines the Bellman error and regularization

$$\mathcal{L}(\theta) = \underbrace{\mathbb{E} \left[(r + \gamma \tanh(W\phi(s'))^\top \theta - \tanh(W\phi(s))^\top \theta)^2 \right]}_{\text{Quadratic in } \theta} + \lambda_\theta \|\theta\|^2.$$

Note that though $\tanh(W\phi(s))$ is nonlinear in $\phi(s)$, $V(s; \theta)$ is linear in θ and hence the Bellman error term is quadratic in θ . We then expand the Bellman error term:

$$\mathbb{E} \left[(r + (\gamma \tanh(W\phi(s'))^\top \theta - \tanh(W\phi(s))^\top \theta))^2 \right] = \theta^\top A \theta - 2\theta^\top b + c, \quad (35)$$

where

$$A = \mathbb{E} \left[(\gamma \tanh(W\phi(s')) - \tanh(W\phi(s))) (\gamma \tanh(W\phi(s')) - \tanh(W\phi(s)))^\top \right], \quad (36)$$

$$b = \mathbb{E} [r(\gamma \tanh(W\phi(s')) - \tanh(W\phi(s)))] \quad (37)$$

$$c = \mathbb{E}[r^2]. \quad (38)$$

Adding the L2-regularization term, the total loss becomes:

$$\mathcal{L}(\theta) = \theta^\top (A + \lambda_\theta I) \theta - 2\theta^\top b + c. \quad (39)$$

Note that the Hessian matrix $H = 2(A + \lambda_\theta I) \succeq 2\lambda_\theta I$. Since $\lambda_\theta > 0$, the matrix $A + \lambda_\theta I$ is positive definite, ensuring that $\mathcal{L}(\theta)$ is $2\lambda_\theta$ -strongly convex. It is well-known that a strongly convex function has exactly one global minimum. The optimal θ^* satisfies:

$$\nabla_\theta \mathcal{L}(\theta^*) = 0 \implies (A + \lambda_\theta I)\theta^* = b.$$

Solving this linear system yields $\theta^* = (A + \lambda_\theta I)^{-1}b$. Then, we show that using gradient descent ensures linear convergence to the global minimum θ^* .

We expand $\mathcal{L}(\theta_2)$ around θ_1 using Taylor's theorem:

$$\mathcal{L}(\theta_2) = \mathcal{L}(\theta_1) + \nabla f(\theta_1)^\top (\theta_2 - \theta_1) + \frac{1}{2}(\theta_2 - \theta_1)^\top \nabla^2 f(\xi)(\theta_2 - \theta_1), \quad (40)$$

where ξ lies on the line segment between θ_1 and θ_2 . Recall that the gradient of the loss function is β -smooth, i.e.,

$$\|\nabla \mathcal{L}(\theta_2) - \nabla \mathcal{L}(\theta_1)\| \leq \beta \|\theta_2 - \theta_1\|. \quad (41)$$

It indicates that the largest eigenvalue of $\nabla^2 \mathcal{L}(\xi)$ is bounded by β . Thus:

$$\frac{1}{2}(\theta_2 - \theta_1)^\top \nabla^2 \mathcal{L}(\xi)(\theta_2 - \theta_1) \leq \frac{\beta}{2} \|\theta_2 - \theta_1\|^2. \quad (42)$$

Substituting back induces:

$$\mathcal{L}(\theta_2) \leq \mathcal{L}(\theta_1) + \nabla \mathcal{L}(\theta_1)^\top (\theta_2 - \theta_1) + \frac{\beta}{2} \|\theta_2 - \theta_1\|^2. \quad (43)$$

Recall that \mathcal{L} is $2\lambda_\theta$ -strongly convex, based on its definition, we have for all θ_1, θ_2 :

$$\mathcal{L}(\theta_2) \geq \mathcal{L}(\theta_1) + \nabla \mathcal{L}(\theta_1)^\top (\theta_2 - \theta_1) + \lambda_\theta \|\theta_2 - \theta_1\|^2. \quad (44)$$

Apply strong convexity at $\theta_1 = \theta^*$, we have

$$\mathcal{L}(\theta) \geq \mathcal{L}(\theta^*) + \underbrace{\nabla \mathcal{L}(\theta^*)^\top (\theta - \theta^*)}_{=0} + \lambda_\theta \|\theta - \theta^*\|^2. \quad (45)$$

Denote $\bar{\lambda} := 2\lambda_\theta$, and we have

$$\mathcal{L}(\theta) - \mathcal{L}(\theta^*) \geq \frac{\bar{\lambda}}{2} \|\theta - \theta^*\|^2. \quad (46)$$

Next, we use the Polyak-Łojasiewicz (PL) inequality (Nesterov, 2013; Karimi et al., 2016), which relates the gradient norm to the function suboptimality,

$$\|\nabla \mathcal{L}(\theta)\|^2 \geq 2\bar{\lambda}(\mathcal{L}(\theta) - \mathcal{L}(\theta^*)). \quad (47)$$

Now we consider the gradient descent with the following form:

$$\theta_{t+1} = \theta_t - \alpha \nabla \mathcal{L}(\theta_t), \quad (48)$$

where α is the step size. Setting $\theta_2 = \theta_{t+1}$ and $\theta_1 = \theta_t$ in Equation 43 and we have

$$\mathcal{L}(\theta_{t+1}) \leq \mathcal{L}(\theta_t) - \alpha \|\nabla \mathcal{L}(\theta_t)\|^2 + \frac{\beta\alpha^2}{2} \|\nabla \mathcal{L}(\theta_t)\|^2 \quad (49)$$

$$= \mathcal{L}(\theta_t) - \alpha \left(1 - \frac{\beta\alpha}{2}\right) \|\nabla \mathcal{L}(\theta_t)\|^2. \quad (50)$$

For $\alpha \leq \frac{1}{\beta}$, the term $\left(1 - \frac{\beta\alpha}{2}\right) \geq \frac{1}{2}$, hence we have

$$\mathcal{L}(\theta_{t+1}) \leq \mathcal{L}(\theta_t) - \frac{\alpha}{2} \|\nabla \mathcal{L}(\theta_t)\|^2. \quad (51)$$

By using Equation 47, we have that $\|\nabla \mathcal{L}(\theta_t)\|^2 \geq \frac{\bar{\lambda}}{2}(\mathcal{L}(\theta_t) - \mathcal{L}(\theta^*))$ and combining it with Equation 51, we have

$$\mathcal{L}(\theta_{t+1}) \leq \mathcal{L}(\theta_t) - \frac{\alpha}{2} \cdot 2\bar{\lambda}(\mathcal{L}(\theta_t) - \mathcal{L}(\theta^*)). \quad (52)$$

This implies that

$$\mathcal{L}(\theta_{t+1}) - \mathcal{L}(\theta^*) \leq \left(1 - \alpha\bar{\lambda}\right) (\mathcal{L}(\theta_t) - \mathcal{L}(\theta^*)). \quad (53)$$

This indicates a linear convergence rate with contraction factor $1 - \alpha\bar{\lambda} = 1 - 2\alpha\lambda_\theta$. For $\alpha = \frac{1}{\beta}$:

$$\mathcal{L}(\theta_t) - \mathcal{L}(\theta^*) \leq \left(1 - \frac{2\lambda_\theta}{\beta}\right)^t (\mathcal{L}(\theta_0) - \mathcal{L}(\theta^*)).$$

Since $0 < \lambda_\theta < \frac{\beta}{2}$, the term $\left(1 - \frac{2\lambda_\theta}{\beta}\right) < 1$, ensuring exponential decay. Hence, we conclude that the weight θ converges to a global minimum θ^* linearly. \square

A.5 PROOF OF THEOREM 5.1

The proof of Theorem 5.1 quite resembles the proof in TD3 (Fujimoto et al., 2018). We show it in the finite MDP setting, where we maintain two tabular value estimates Q^A, Q^B . At each timestep t , we select action a^* via $a^* = \arg \max_a Q_t^A(s, a)$ and calculate the target value of the convex Q-learning,

$$y = r + \gamma (\lambda \times \min(Q^A(s', a^*), Q^B(s', a^*)) + (1 - \lambda) \times \max(Q^A(s', a^*), Q^B(s', a^*))). \quad (54)$$

Then, we update the value estimates by using the vanilla Q-learning update formula:

$$\begin{aligned} Q_{t+1}^A(s, a) &\leftarrow Q_t^A(s, a) + \alpha_t(y - Q_t^A(s, a)), \\ Q_{t+1}^B(s, a) &\leftarrow Q_t^B(s, a) + \alpha_t(y - Q_t^B(s, a)), \end{aligned} \quad (55)$$

where α_t is the learning rate. We also need to use a well-known lemma that is adopted in (Fujimoto et al., 2018)².

Lemma A.5. Consider a stochastic process $(\zeta_t, \Delta_t, F_t), t \geq 0$ where $\zeta_t, \Delta_t, F_t : X \mapsto \mathbb{R}$ satisfy the equation:

$$\Delta_{t+1}(x_t) = (1 - \zeta_t(x_t))\Delta_t(x_t) + \zeta_t(x_t)F_t(x_t), \quad (56)$$

where $x_t \in X$ and $t = 0, 1, 2, \dots$. Let P_t be a sequence of increasing σ -fields such that ζ_0 and Δ_0 are P_0 -measurable and ζ_t, Δ_t and F_{t-1} are P_t -measurable, $t = 1, 2, \dots$. Assume the following conditions hold: (1) The set X is finite; (2) $\zeta_t(x_t) \in [0, 1]$, $\sum_t \zeta_t(x_t) = \infty$, $\sum_t (\zeta_t(x_t))^2 < \infty$ with probability 1 and $\forall x \neq x_t : \zeta_t(x) = 0$; (3) $\|\mathbb{E}[F_t | P_t]\| \leq \kappa \|\Delta_t\| + c_t$, where $\|\cdot\|$ denotes maximum norm, $\kappa \in [0, 1)$ and c_t converges to 0 with probability 1; (4) $\text{Var}[F_t(x_t) | P_t] \leq C(1 + \|\Delta_t\|)^2$, where C is some constant. Then Δ_t converges to 0 with probability 1.

Then we are ready to show the following theorem.

Theorem A.6 (Theorem 5.1 restated). Given the following conditions: (1) each state-action pair is sampled an infinite number of times; (2) the MDP is finite; (3) $\gamma \in [0, 1)$; (4) Q values are stored in a look-up table; (5) the learning rates satisfy $\alpha_t(s, a) \in [0, 1]$, $\sum_t \alpha_t(s, a) = \infty$, $\sum_t (\alpha_t(s, a))^2 < \infty$ with probability 1 and $\alpha_t(s, a) = 0, \forall (s, a) \neq (s_t, a_t)$; (6) $\text{Var}[r(s, a)] < \infty, \forall s, a$; (7) the Q-values receive an infinite number of updates, then for any $\lambda \in (0, 1]$, the Convex Q-learning converges to the optimal value function Q^* as defined by the Bellman optimality equation with probability 1.

Proof. To apply Lemma A.5, we set $P_t = \{Q_0^A, Q_0^B, s_0, a_0, \dots, s_t, a_t\}$, $X = \mathcal{S} \times \mathcal{A}$, $\zeta_t = \alpha_t$, and $\Delta_t = Q_t^A - Q^*$. Notice that the conditions (1) and (2) of Lemma A.5 hold due to the assumed conditions (2) and (5) in our theorem, respectively. Denote $a^* = \arg \max_a Q^A(s_{t+1}, a)$, we have

$$\begin{aligned} &\Delta_{t+1}(s_t, a_t) \\ &= Q_{t+1}^A(s_t, a_t) - Q^*(s_t, a_t) \\ &= (1 - \alpha_t) \underbrace{(Q_t^A(s_t, a_t) - Q^*(s_t, a_t))}_{=\Delta_t} + \alpha_t(y - Q^*(s_t, a_t)) \\ &= (1 - \alpha_t)\Delta_t + \\ &\alpha_t \underbrace{(r_t + \gamma[\lambda \min(Q_t^A(s_{t+1}, a^*), Q_t^B(s_{t+1}, a^*)) + (1 - \lambda) \max(Q_t^A(s_{t+1}, a^*), Q_t^B(s_{t+1}, a^*))] - Q^*(s_t, a_t)}_{:=F_t(s_t, a_t)} \\ &= (1 - \alpha_t)\Delta_t + \alpha_t F_t(s_t, a_t). \end{aligned} \quad (57)$$

For the defined $F_t(s_t, a_t)$, the condition (4) of the lemma holds by the condition (6) in our theorem. Furthermore, we have

$$\begin{aligned} &F_t(s_t, a_t) \\ &= r_t + \gamma[\lambda \min(Q_t^A(s_{t+1}, a^*), Q_t^B(s_{t+1}, a^*)) \\ &\quad + (1 - \lambda) \max(Q_t^A(s_{t+1}, a^*), Q_t^B(s_{t+1}, a^*))] - Q^*(s_t, a_t) \\ &= r_t + \gamma[\lambda \min(Q_t^A(s_{t+1}, a^*), Q_t^B(s_{t+1}, a^*)) \\ &\quad + (1 - \lambda) \max(Q_t^A(s_{t+1}, a^*), Q_t^B(s_{t+1}, a^*))] - Q^*(s_t, a_t) + \gamma Q_t^A(s_{t+1}, a^*) - \gamma Q_t^A(s_{t+1}, a^*) \\ &= F_t^Q(s_t, a_t) + c_t, \end{aligned} \quad (58)$$

where we define $F_t^Q(s_t, a_t)$ and c_t below,

$$\begin{aligned} F_t^Q(s_t, a_t) &= r_t + \gamma Q_t^A(s_{t+1}, a^*) - Q^*(s_t, a_t), \\ c_t &= \gamma[\lambda \min(Q_t^A(s_{t+1}, a^*), Q_t^B(s_{t+1}, a^*)) + (1 - \lambda) \max(Q_t^A(s_{t+1}, a^*), Q_t^B(s_{t+1}, a^*))] \\ &\quad - \gamma Q_t^A(s_{t+1}, a^*). \end{aligned} \quad (59)$$

²The proof can be found in <https://link.springer.com/content/pdf/10.1023/a:1007678930559.pdf>

Note that $\mathbb{E}[F_t^Q | P_t] \leq \gamma \|\Delta_t\|$ is a well-known result. It remains to show that c_t converges to 0 with probability 1. Denote $\Delta_t^{BA}(s_t, a_t) = Q_t^B(s_t, a_t) - Q_t^A(s_t, a_t)$, then c_t converges to 0 if $\Delta_t^{BA}(s_t, a_t)$ converges to 0, which holds for any $\lambda \in (0, 1]$. We then aim at showing that Δ_t^{BA} converges to 0 with probability 1. Based on the definition and the update rule of Q-learning, we have

$$\begin{aligned}\Delta_{t+1}^{BA}(s_t, a_t) &= Q_{t+1}^B(s_t, a_t) - Q_{t+1}^A(s_t, a_t) \\ &= Q_t^B(s_t, a_t) + \alpha_t(y - Q_t^B(s_t, a_t)) - Q_t^A(s_t, a_t) - \alpha_t(y - Q_t^A(s_t, a_t)) \\ &= (1 - \alpha_t)(Q_t^B(s_t, a_t) - Q_t^A(s_t, a_t)) \\ &= (1 - \alpha_t)\Delta_t^{BA}(s_t, a_t).\end{aligned}\quad (60)$$

We then conclude that Δ_t^{BA} converges to 0, indicating that the condition (3) of Lemma A.5 is satisfied. Then, by using Lemma A.5, we have Q^A converges to Q^* with probability 1. Similarly, we get the convergence of Q^B by defining $\Delta_t = Q_t^B - Q^*$ and following the same procedure above. Combining these results, the proof is completed. \square

B PSEUDO-CODES FOR CIR

We present the detailed pseudo-code for CIR in Algorithm 1.

Algorithm 1 Constrained Initial Representations (CIR)

```

1: Initialize critic networks  $Q_{\theta_1}, Q_{\theta_2}$  and actor network  $\pi_\phi$  with random parameters
2: Initialize target networks  $\theta'_1 \leftarrow \theta_1, \theta'_2 \leftarrow \theta_2$  and replay buffer  $\mathcal{D} = \{\}$ 
3: Initialize temperature coefficient  $\alpha$ , target update rate  $\tau$ , number of interaction steps  $T$ 
4: Set value coefficient  $\lambda$ , normalization parameter  $c$ , SMR ratio  $M$ 
5: for  $t = 1$  to  $T$  do
6:   Take one action  $a_t \sim \pi_\phi(\cdot | s_t)$  and observe reward  $r_t$ , new state  $s'_{t+1}$ 
7:   Store transitions in the replay buffer, i.e.,  $\mathcal{D} \leftarrow \mathcal{D} \cup \{(s_t, a_t, r_t, s'_{t+1})\}$ 
8:   Sample a mini-batch  $B = \{(s, a, r, s')\} \sim \mathcal{D}$ 
9:   for  $m = 1$  to  $M$  do
10:    Compute the  $Q$  target using the convex Q-learning approach:

$$y = r + \gamma \left( \lambda \times \min_{i \in \{1, 2\}} Q_{\theta'_i}(s', a') + (1 - \lambda) \times \max_{i \in \{1, 2\}} Q_{\theta'_i}(s', a') - \alpha \log \pi_\phi(a' | s') \right),$$

    where  $a' \sim \pi_\phi(\cdot | s')$ 
11:    Update  $\theta_i$  with gradient descent using  $\nabla_{\theta_i} \frac{1}{|B|} \sum_{(s, a, r, s') \sim B} (Q_{\theta_i}(s, a) - y)^2$ 
12:    Update target networks:  $\theta'_i \leftarrow \tau \theta_i + (1 - \tau) \theta'_i$ 
13:    Update actor  $\phi$  with  $\nabla_\phi \frac{1}{|B|} \sum_{s \in B} \left( \frac{1}{2} \sum_{j=1}^2 Q_{\theta_j}(s, \tilde{a}) - \alpha \log \pi_\phi(\tilde{a} | s) \right), \tilde{a} \sim \pi_\phi(\cdot | s)$ 
14:  end for
15: end for

```

We further present below the detailed comparison of CIR against prior methods. Different from prior methods, we explore a novel way of constraining initial representations to improve sample efficiency, where CIR involves different architecture components and algorithm components.

Table 2: Architecture and algorithmic comparison between CIR and prior methods.

Algorithm	Architecture Components	Algorithm Components
BRO	LayerNorm, residual connection, weight decay, parameter reset	Distributional Q-learning, Huber loss, dual policy exploration, UTD
SimBa	RSNorm, pre-layer normalization, post-layer normalization, residual connection, weight decay	single/double Q-learning, UTD
CIR (ours)	Tanh, AvgRNorm, LayerNorm, skip connection	SMR, Convex Q-learning

C ENVIRONMENT DETAILS

In this part, we give detailed environment descriptions for selected benchmarks. We mainly consider DMC suite (Tassa et al., 2018), HumanoidBench (Sferrazza et al., 2024), and ODRL (Lyu et al., 2024c). The visualization results of selected tasks from these benchmarks can be found in Figure 3.

DeepMind Control suite. DeepMind Control suite (Tassa et al., 2018) (DMC suite) is a popular continuous control benchmark in RL, which utilizes proprioceptive states as the observation space. It contains a wide range of continuous control tasks with varying complexities, involving both low-dimensional tasks (the state dimension can give only 3, the action dimension can give only 1) and high-dimensional tasks (the state dimension can give 223, the action dimension can give 38). The total reward of each episode in DMC suite is limited to 1000, making it comparatively easy to aggregate results. We choose 27 DMC suite tasks for evaluation, including 20 DMC suite easy & medium tasks, and 7 hard tasks (humanoid and dog tasks). We show in Table 3 the detailed information (state space dimension and action space dimension) of the adopted DMC easy & medium tasks. We also present the detailed task name, state space information, and action space information of DMC hard tasks in Table 4. For all DMC suite tasks, we use the average episode return as the performance metric. We run DMC easy & medium tasks for 500K environment steps and hard tasks for 1M environment steps. The action repeat for all DMC tasks is set to be 2.

Table 3: Detailed state and action space dimensions for DMC easy and medium tasks.

Task	Observation dimension	Action dimension
Acrobot Swingup	6	1
Cartpole Balance	5	1
Cartpole Balance Sparse	5	1
Cartpole Swingup	5	1
Cartpole Swingup Sparse	5	1
Cheetah Run	17	6
Finger Spin	9	2
Finger Turn Easy	12	2
Finger Turn Hard	12	2
Fish Swim	24	5
Hopper Hop	15	4
Hopper Stand	15	4
Pendulum Swingup	3	1
Quadruped Run	78	12
Quadruped Walk	78	12
Reacher Easy	6	2
Reacher Hard	6	2
Walker Run	24	6
Walker Stand	24	6
Walker Walk	24	6

Table 4: **Detailed state and action space dimensions for DMC hard tasks.**

Task	Observation dimension	Action dimension
Dog Run	223	38
Dog Trot	223	38
Dog Stand	223	38
Dog Walk	223	38
Humanoid Run	67	24
Humanoid Stand	67	24
Humanoid Walk	67	24

HumanoidBench. HumanoidBench (Sferrazza et al., 2024) is a high-dimensional simulated robot learning benchmark built upon the Unitree H1 humanoid robot. HumanoidBench provides an accessible, fast, safe, and inexpensive testbed for the field of robot learning research. It demonstrates a variety of challenges in learning for autonomous humanoid robots, including the intricate control of robots with complex dynamics, sophisticated coordination among various body parts, and handling long-horizon complex tasks. It features a variety of challenging whole-body manipulation tasks with dexterous hands and locomotion tasks. HumanoidBench offers a promising platform for facilitating prompt verification of algorithms and ideas in humanoid robots. Following SimBa (Lee et al., 2025a), we consider 14 locomotion tasks without dexterous hands. The observation dimension of these tasks ranges from 51 to 77, and the action space dimension of these tasks gives 19. We run HumanoidBench tasks for 2M environment steps with action repeat 2. Note that HumanoidBench tasks have quite distinct average episode returns for different tasks. To better aggregate results, we use *normalized return* as the metric, which normalizes the performance score of the agent by their corresponding task success score. Denote the task success score of task i from HumanoidBench as S_i , the average episode return of the agent in the task i as R_i , then the normalized return NS_i for task i is computed by:

$$NS_i = \frac{R_i}{S_i} \times 1000. \quad (61)$$

We summarize the information on the state dimensions, action dimensions, and the corresponding task success scores of our selected tasks from HumanoidBench in Table 5.

Table 5: **Detailed state, action space dimensions and task success scores for HumanoidBench tasks.**

Task	Observation dimension	Action dimension	Task success score
Balance Hard	77	19	800
Balance Simple	64	19	800
Crawl	51	19	700
Hurdle	51	19	700
Maze	51	19	1200
Pole	51	19	700
Reach	57	19	12000
Run	51	19	700
Sit Simple	51	19	750
Sit Hard	64	19	750
Slide	51	19	700
Stair	51	19	700
Stand	51	19	800
Walk	51	19	700

ODRL. ODRL (Lyu et al., 2024c) is a benchmark for off-dynamics RL, where the agent can interact with a source domain (with sufficient data) and a target domain (with a limited budget) at the same time, and it aims at enhancing its performance in the target domain by using source domain data. There exist dynamics discrepancies between the source domain and the target domain, therefore the source domain data is OOD for training policies in the target domain. We adopt 8 tasks

from ODRL, which cover 4 kinds of dynamics shifts between the source domain and the target domain (friction/gravity/kinematic/morphology). All methods are run for 1M environment steps in the source domain, and the agent can interact with the target domain every 10 source domain steps. The action repeat is set to be 1. Following ODRL, we calculate the normalized return of the agent for better comparison, which is given by:

$$NS = \frac{J_\pi - J_r}{J_e - J_r} \times 100, \quad (62)$$

where J_π is the episode return of the learned policy, J_r is the return of the random policy, J_e is the return of the expert policy. The reference random policy scores and expert policy scores for each task are outlined in Table 6. We also present in Table 7 the detailed numerical result comparison between CIR and other off-dynamics RL baselines on ODRL tasks.

Table 6: Reference scores in ODRL tasks.

Task	Reference random policy score	Reference expert policy score
walker2d-friction-0.5	10.08	4229.348
walker2d-friction-5.0	10.08	4988.835
ant-friction-0.5	-325.6	8301.338
walker2d-gravity-0.5	10.08	5194.713
ant-gravity-0.5	-325.6	4317.065
ant-gravity-5.0	-325.6	6226.89
ant-kinematic-anklejnt-medium	-325.6	5139.832
ant-morph-allegs-hard	-325.6	5139.832

Table 7: Numerical results of CIR against off-dynamics RL baselines on ODRL tasks. We bold the best mean results.

Task	SAC	DARC	PAR	CIR (ours)
walker2d-friction-0.5	3761.6 ± 671.2	4062.2 ± 727.5	4074.5 ± 225.8	4089.1 ± 628.4
walker2d-friction-5.0	319.9 ± 21.0	291.6 ± 36.2	481.2 ± 199.6	319.1 ± 67.6
ant-friction-0.5	5664.5 ± 274.7	6230.9 ± 180.8	7135.0 ± 359.5	7716.6 ± 112.3
walker2d-gravity-0.5	2746.5 ± 638.2	3112.6 ± 367.7	3328.5 ± 356.7	3759.8 ± 419.9
ant-gravity-0.5	682.9 ± 247.6	110.1 ± 60.4	1737.8 ± 634.4	1203.9 ± 627.4
ant-gravity-5.0	4470.0 ± 248.5	1312.3 ± 236.1	4668.6 ± 419.1	4970.3 ± 271.6
ant-kinematic-anklejnt-medium	6074.2 ± 212.4	5535.5 ± 393.6	5959.4 ± 305.9	6221.3 ± 231.6
ant-morph-allegs-hard	911.2 ± 38.8	440.8 ± 132.6	910.9 ± 19.7	930.5 ± 20.6

D HYPERPARAMETER SETUP AND EXPERIMENTAL DETAILS

D.1 HYPERPARAMETER SETUP

We present the detailed hyperparameter setup for CIR across all tasks in Table 8.

Table 8: **Hyperparameter setup for CIR.** For most hyperparameters, we follow the hyperparameter setup used in prior works (e.g., TD3, SAC) and do not alter them.

Hyperparameter	Value
Actor network	(512, 512)
Actor architecture type	vanilla MLP
Number of hidden layers in actor	2
Critic network	(512, 512)
Critic architecture type	U-shape
Number of up-sampling layers in critic	2
Number of down-sampling layers in critic	2
Batch size	256
Learning rate	3×10^{-4}
Optimizer	Adam (Kingma & Ba, 2014)
Discount factor	Heuristic
Replay buffer size	10^6
Warmup steps	5×10^3
Nonlinearity	elu
Target update rate	5×10^{-3}
Entropy target	$-\dim(\mathcal{A})$
Entropy auto-tuning	True
Maximum log std	2
Minimum log std	-20
SMR ratio M	2
Convex Q-learning coefficient λ	0.3 (DMC, ODRL), 1.0 (HumanoidBench)
AvgRNorm coefficient c	0.1

D.2 EXPERIMENTAL DETAILS

In this part, we introduce the detailed experiment setup in the main text. We run CIR for 10 random seeds, and the remaining baseline results are taken directly from the SimBa paper (Lee et al., 2025a)³. In Section 6.3, we conduct an ablation study on the following tasks: acrobot swingup, finger spin, finger turn easy, finger turn hard, hopper hop, hopper stand, walker run, humanoid run, humanoid stand, humanoid walk, dog run, dog walk, dog stand, dog trot, where we include all 7 DMC hard tasks, incurring a total of 14 tasks.

In Section 6.4, we utilize the following DMC tasks: acrobot swingup, cheetah run, fish swim, hopper hop, hopper stand, walker run, humanoid run, humanoid stand, humanoid walk for scaling experiments.

³A full list of results can be found in <https://github.com/SonyResearch/simba/tree/master/results>

E EXTENDED EXPERIMENTS AND RESULTS

In this section, we provide missing numerical results, more ablation studies, and scaling experiments to further demonstrate the scaling ability of our proposed CIR method and verify our design choices.

E.1 MISSING DETAILED NUMERICAL RESULTS

We first present the detailed numerical results of CIR against the following variants in Table 9:

- CIR (sigmoid): which replaces the Tanh function in CIR with the sigmoid function. We note that Tanh is equivalent to sigmoid to some extent, i.e., $\tanh(x) = \frac{e^x - e^{-x}}{e^x + e^{-x}} = \frac{2}{1+e^{-2x}} - 1 = 2\text{sigmoid}(2x) - 1$.
- CIR (softmax): which replaces the Tanh function in CIR with the softmax function
- CIR (layernorm): which replaces the Tanh function in CIR with Layer Normalization (removing γ and β in layer normalization for scaling).
- CIR (noSC): which removes the skip connection module in CIR.

These results correspond to the ablation study in Figure 5 (right). Intuitively, sigmoid and softmax may not be good candidates for this since they do not preserve signs. The results show that CIR (sigmoid) and CIR (softmax) exhibit poor performance on numerous tasks, which validates the rationality and advantages of using Tanh. Please note that we are not arguing that Tanh is the best choice; it is fully possible that there exists a better normalizer than Tanh, which we believe can be an interesting topic to study.

Table 9: Numerical results of CIR against its variants. SC denotes skip connection.

Task	CIR (Tanh)	CIR (sigmoid)	CIR (softmax)	CIR (layernorm)	CIR (no SC)
acrobot-swingup	443.5±79.0	132.0±82.8	72.5±84.5	251.4±22.4	385.1±62.9
cartpole-balance	998.1±2.4	996.1±2.7	999.0±0.8	999.2±0.4	998.9±1.1
cartpole-balance-sparse	999.6±1.2	1000.0±0.0	1000.0±0.0	914.6±147.9	812.4±280.4
cartpole-swingup	875.2±4.5	877.7±1.5	872.9±6.5	880.9±0.5	880.8±0.4
cartpole-swingup-sparse	839.6±12.3	750.7±72.6	714.0±113.2	833.9±14.1	797.7±87.1
cheetah-run	747.0±73.2	575.9±80.5	530.6±11.9	724.1±70.1	762.8±25.5
finger-spin	940.0±35.6	921.4±3.5	732.3±143.3	888.4±158.7	779.5±111.6
finger-turn-easy	892.5±88.9	764.8±135.4	172.2±120.6	920.4±46.9	862.4±111.5
finger-turn-hard	888.4±74.3	310.4±204.7	75.9±68.4	916.8±43.9	894.4±74.0
fish-swim	781.8±21.9	633.5±65.4	63.1±28.4	788.4±4.7	758.7±25.6
hopper-hop	280.1±87.9	90.9±6.1	8.9±15.9	250.9±88.2	278.1±172.8
hopper-stand	822.0±211.1	830.0±36.7	4.8±6.3	796.4±217.5	741.3±288.9
pendulum-swingup	838.0±27.9	488.7±400.5	793.5±39.6	814.7±42.3	844.5±26.1
quadruped-run	807.0±31.7	524.9±57.1	457.0±25.7	834.5±53.5	748.8±42.4
quadruped-walk	933.8±18.6	913.9±32.3	864.3±53.7	946.4±6.7	948.3±12.0
reacher-easy	974.1±29.4	977.3±6.6	954.3±50.0	979.3±3.5	987.0±1.2
reacher-hard	954.2±36.9	955.7±37.6	934.4±53.1	965.6±11.5	927.5±52.3
walker-run	810.0±14.0	584.6±86.4	566.6±54.7	785.5±1.3	784.8±16.9
walker-walk	973.9±3.1	967.6±4.4	969.0±6.2	972.0±2.8	972.2±4.2
walker-stand	986.7±5.0	973.1±20.5	982.1±3.9	987.6±3.7	967.2±12.8
Average Return	839.3	713.5	588.4	822.6	806.6

Furthermore, we investigate how beneficial Tanh would be when adopted by simpler algorithms. To that end, we run experiments on 20 DMC easy & medium tasks. We use the following baselines:

- SAC+Tanh, where we constrain the initial representations in SAC with vanilla Tanh.
- SAC+Tanh+Norm, where we add AvgRNorm and LayerNorm before constraining the initial representation while keeping the downstream network architecture unchanged.

We summarize the results in Table 10. We find that SAC+Tanh incurs a performance drop on many tasks, despite the fact that Tanh still improves its average performance against vanilla SAC, indicating that Tanh alone can still be beneficial to simple algorithms. By adding normalization

methods, the performance of SAC+Tanh improves drastically and significantly outperforms vanilla SAC, verifying our Theorem 4.5 and showing that many components (Tanh, normalization, etc.) work altogether to enable CIR to perform well. Furthermore, SAC+Tanh+Norm underperforms CIR on numerous tasks, which validates our design choices.

Table 10: Numerical results of CIR against SAC variants.

Task	SAC	SAC+Tanh	SAC+Tanh+Norm	CIR
acrobot-swingup	57.6	18.2 \pm 17.2	5.5 \pm 4.3	443.5 \pm 79.0
cartpole-balance	998.8	999.8 \pm 0.1	999.8 \pm 0.0	998.1 \pm 2.4
cartpole-balance-sparse	1000.0	1000.0 \pm 0.0	1000.0 \pm 0.0	999.6 \pm 1.2
cartpole-swingup	863.2	880.4 \pm 1.2	876.7 \pm 7.2	875.2 \pm 4.5
cartpole-swingup-sparse	780.0	650.4 \pm 326.0	788.9 \pm 32.9	839.6 \pm 12.3
cheetah-run	716.4	642.2 \pm 69.5	749.1 \pm 63.1	747.0 \pm 73.2
finger-spin	814.7	832.7 \pm 44.7	851.7 \pm 21.2	940.0 \pm 35.6
finger-turn-easy	903.1	765.4 \pm 197.7	791.6 \pm 109.6	892.5 \pm 88.9
finger-turn-hard	775.2	798.4 \pm 155.1	619.9 \pm 244.9	888.4 \pm 74.3
fish-swim	462.7	730.5 \pm 37.6	639.5 \pm 116.3	781.8 \pm 21.9
hopper-hop	159.4	52.4 \pm 44.6	136.5 \pm 89.3	280.1 \pm 87.9
hopper-stand	845.9	468.4 \pm 256.3	528.0 \pm 334.2	822.0 \pm 211.1
pendulum-swingup	476.6	676.0 \pm 293.3	833.3 \pm 29.1	838.0 \pm 27.9
quadruped-run	116.9	565.6 \pm 114.1	837.8 \pm 52.3	807.0 \pm 31.7
quadruped-walk	147.8	777.8 \pm 296.4	938.1 \pm 20.5	933.8 \pm 18.6
reacher-easy	951.8	981.3 \pm 3.9	981.4 \pm 2.4	974.1 \pm 29.4
reacher-hard	959.6	912.4 \pm 54.0	968.8 \pm 2.2	954.2 \pm 36.9
walker-run	629.4	638.7 \pm 56.7	683.2 \pm 36.5	810.0 \pm 14.0
walker-walk	956.7	961.2 \pm 7.1	938.0 \pm 55.4	973.9 \pm 3.1
walker-stand	972.6	972.1 \pm 1.5	981.0 \pm 6.8	986.7 \pm 5.0

Furthermore, we replace the UTD replay method in SimBa with SMR in the official SimBa code-base, giving birth to SimBa (SMR). This aims at understanding the importance of SMR and making a fair comparison between CIR and SimBa. We run SimBa (SMR) on 20 DMC suite easy and medium tasks. We compare CIR (SMR) against SimBa (UTD) and SimBa (SMR) below in Table 11. We run SimBa (SMR) for 5 seeds. The results show that SMR can boost the performance of SimBa on some tasks, while it can also incur performance degradation on many tasks compared to UTD. It seems that SMR can work better by combining it with CIR. The reasons can lie in different network architectures and algorithmic components between CIR and SimBa.

E.2 MORE ABLATION STUDY

Following the main text, we adopt 7 DMC medium tasks and 7 DMC hard tasks (specified in Appendix D.2) and consider the following CIR variants: (i) **ActorLN**, which incorporates layer normalization to the actor network; (ii) **ActorCIR**, which adopts the same network architecture for the actor as the critics in CIR; (iii) **Res**, which substitutes skip connections for residual connections; (iv) **NoEnt**, which removes the entropy term in Equation 10. We summarize the overall results in Figure 7, where we report the percent CIR performance (% CIR performance) of these variants. If the percent CIR performance exceeds 100, it indicates that the variant outperforms CIR, and underperforms CIR if it is smaller than 100.

On the actor network architecture. We find that both **ActorLN** and **ActorCIR** underperform CIR, indicating that either adding layer normalization to the actor network or replacing the plain MLP network with the critics' network architecture in CIR is not effective. A similar phenomenon is observed in BRO (Nauman et al., 2024). The results undoubtedly support our design choice in Section 5.2.

On the critic network architecture. We find that **Res** achieves similar performance as CIR on DMC hard tasks but exhibits inferior performance on medium tasks. This verifies our design choice on the U-shape network.

Table 11: Comparison of CIR against SimBa with SMR.

Task	CIR (SMR)	SimBa (UTD)	SimBa (SMR)
acrobot-swingup	443.5 \pm 79.0	331.6	212.4 \pm 78.1
cartpole-balance	998.1 \pm 2.4	999.1	997.5 \pm 1.9
cartpole-balance-sparse	999.6 \pm 1.2	940.5	993.3 \pm 11.6
cartpole-swingup	875.2 \pm 4.5	866.5	872.2 \pm 6.1
cartpole-swingup-sparse	839.6 \pm 12.3	824.0	820.0 \pm 14.6
cheetah-run	747.0 \pm 73.2	815.0	716.2 \pm 17.4
finger-spin	940.0 \pm 35.6	778.8	741.4 \pm 121.5
finger-turn-easy	892.5 \pm 88.9	881.3	874.8 \pm 13.1
finger-turn-hard	888.4 \pm 74.3	860.2	885.8 \pm 30.6
fish-swim	781.8 \pm 21.9	786.7	268.5 \pm 58.4
hopper-hop	280.1 \pm 87.9	326.7	309.1 \pm 72.4
hopper-stand	822.0 \pm 211.1	811.8	737.4 \pm 191.4
pendulum-swingup	838.0 \pm 27.9	824.5	609.9 \pm 354.5
quadruped-run	807.0 \pm 31.7	883.7	800.7 \pm 39.8
quadruped-walk	933.8 \pm 18.6	953.0	954.0 \pm 8.7
reacher-easy	974.1 \pm 29.4	972.2	711.8 \pm 78.5
reacher-hard	954.2 \pm 36.9	966.0	803.7 \pm 142.7
walker-run	810.0 \pm 14.0	687.2	702.0 \pm 14.2
walker-walk	973.9 \pm 3.1	970.7	972.5 \pm 3.2
walker-stand	986.7 \pm 5.0	983.0	977.4 \pm 0.9

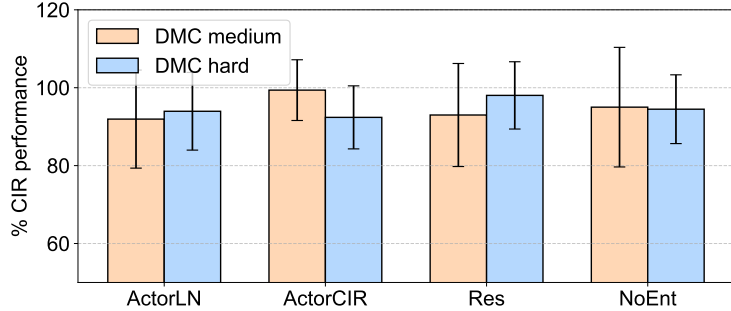


Figure 7: **Extended ablation study.** We report % CIR performance of each variant and aggregate their performance across all tasks. The results are averaged across five seeds.

On algorithmic components. The results show that excluding the entropy term in the target value has a minor influence on the performance of CIR. It is recommended to keep the entropy term in the target value.

We consider the following variants of CIR to further verify our design choices, (i) **NoInputLN**, where there is no layer normalization module at the initial layer, i.e., Equation 7 becomes $\mathbf{z}_t = \tanh(\text{AvgRNorm}(\text{Linear}(\mathbf{o}_t)))$; (ii) **NoAvgRNorm**, which removes the AvgRNorm module in CIR, i.e., Equation 7 becomes $\mathbf{z}_t = \tanh(\text{LayerNorm}(\text{Linear}(\mathbf{o}_t)))$; (iii) **NoInputNorm**, where we remove both AvgRNorm and layer normalization in the initial layer, i.e., Equation 7 becomes $\mathbf{z}_t = \tanh(\text{Linear}(\mathbf{o}_t))$; (iv) **MaxRNorm**, where we replace the AvgRNorm module in the initial layer with the maximum representation normalization, $\text{MaxRNorm}(\mathbf{x}) = \frac{\mathbf{x}}{\text{Max}(\tilde{\mathbf{x}})}$, $\tilde{\mathbf{x}} = |\mathbf{x}|$, where

$\text{Max}(\cdot)$ is the maximum operator; (v) **AllAvgRNorm**, which adds the AvgRNorm module after the layer normalization on all layers; (vi) **Orthoini**, which uses orthogonal initialization for the critic network; (vii) **WD**, which adopts weight decay for the optimizer of the critic network; (viii) **AvgQ**, where we use the average Q learning for calculating the target value ($\lambda = 0.5$ in Equation 10).

To comprehensively compare the performance of CIR against these variants, we run experiments on 9 DMC easy & medium tasks, and 3 DMC hard tasks. This amounts to a total of 12 tasks. The

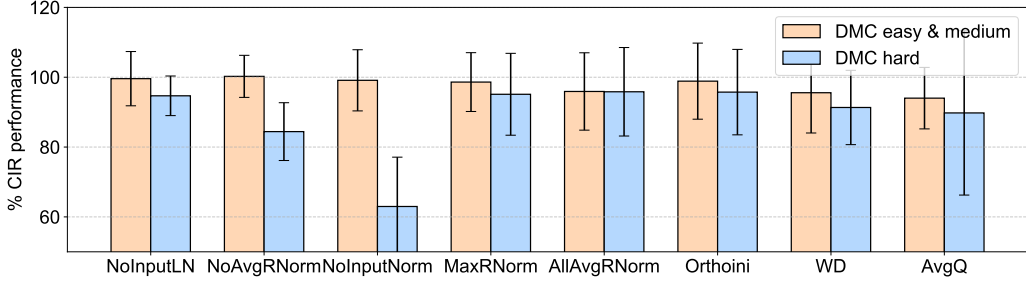


Figure 8: **Extended ablation study.** Following the main text, we report % CIR performance of each variant and aggregate their performance across all tasks. We use five random seeds for each variant.

full list of the selected tasks gives: acrobot swingup, cheetah run, finger spin, finger turn easy, finger turn hard, fish swim, hopper hop, hopper stand, walker run, humanoid run, humanoid stand, humanoid walk.

Following the main text, we also report % CIR performance of these variants at the final environment step. The empirical results can be found in Figure 8.

It turns out that both layer normalization and the AvgRNorm modules are critical to CIR, especially on complex tasks like humanoid. Adopting MaxRNorm or orthogonal initialization leads to a similar performance as the vanilla CIR on DMC easy & medium tasks, but slightly inferior performance on hard tasks. **WD** and **AvgQ**, however, can impede the performance improvement of the agent. The above evidence clearly verifies our design choices in the CIR framework.

Furthermore, we are interested in investigating how sensitive CIR is to the choices of the AvgRNorm parameter c . In CIR, we set $c = 0.1$ by default. Intuitively, using a larger c is not preferred both theoretically and empirically, since our theoretical analysis often requires a small c , and using a large c can make the resulting representation element lie in the gradient vanishing region of the Tanh function, and harm the performance of the agent eventually. We then conduct experiments on DMC tasks with varying c , $c \in \{0.01, 0.1, 0.2, 0.5, 1.0\}$.

To be specific, we run CIR with different choices of c on the following tasks: acrobot swingup, cheetah run, fish swim, hopper hop, hopper stand, walker run, dog run, dog stand, dog walk, humanoid run, humanoid stand, humanoid walk. These tasks include 6 DMC easy & medium tasks and 6 DMC hard tasks, which we believe can reveal how sensitive CIR is to the choices of c under varying task complexities. We summarize the empirical results in Figure 9 where we report the average episode return in conjunction with the aggregated standard deviations (averaged across all environments). The results on DMC easy & medium tasks show that CIR is comparatively insensitive to c on those tasks, while the results in DMC hard tasks show that using a large c can incur a significant performance drop, verifying our claims above. We then use $c = 0.1$ by default across all tasks.

E.3 MORE SCALING RESULTS

In this part, we first investigate the performance of CIR under distinct critic network depth by using fewer or more up-sampling layers and down-sampling layers in the U-shape network. Denote the number of up-sampling layers as L , we compare the performance of CIR under $L \in \{1, 2, 3\}$, where $L = 1$ indicates that there is only 1 up-sampling layer and 1 down-sampling layer, while $L = 3$ means that there are 3 up-sampling and down-sampling layers, respectively (CIR adopts $L = 2$ by default). We use 6 DMC easy & medium tasks, and 7 DMC hard tasks for experiments. The complete task list includes: acrobot swingup, cheetah run, fish swim, hopper hop, hopper stand, walker run, dog run, dog trot, dog stand, dog walk, humanoid run, humanoid stand, humanoid walk.

We report the aggregated average performance along with the aggregated standard deviations of CIR under different equivalent environment steps in Figure 10 (left). The results show that using fewer

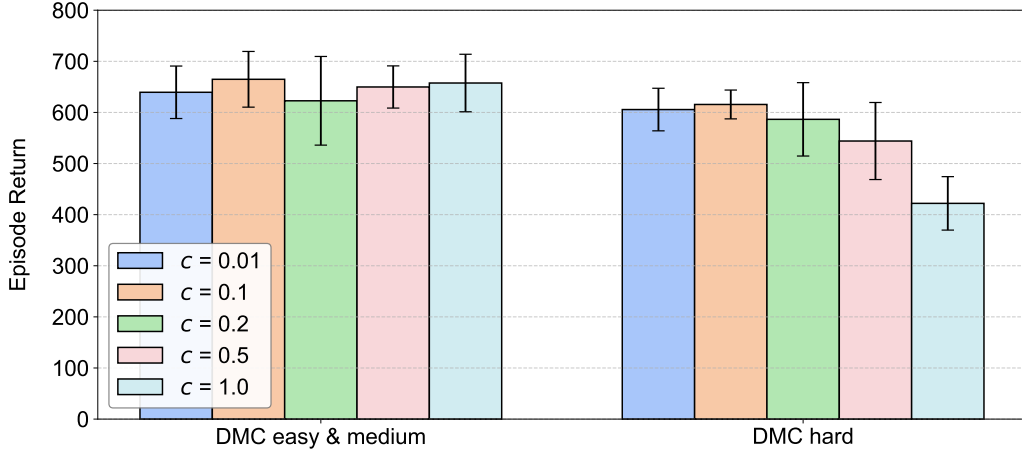


Figure 9: **Parameter study on AvgRNorm.** We conduct experiments on numerous DMC tasks to investigate the influence of the introduced hyperparameter c . We report the aggregated average performance along with the aggregated standard deviations. We use five random seeds.

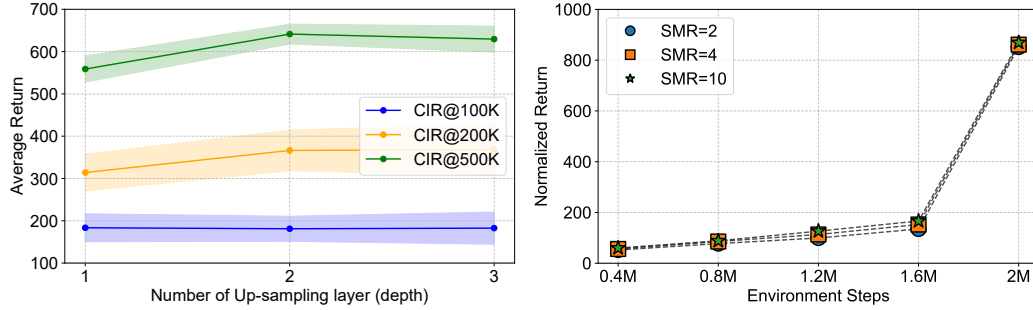


Figure 10: **Extended scaling results of CIR.** We include the scaling results on network depth (**left**) and the SMR ratio (**right**). We report the aggregated average return results for DMC tasks and aggregated normalized return results for HumanoidBench tasks. All results are obtained by averaging across five different seeds and the shaded region captures the standard deviation.

up-sampling layers can incur a performance drop while increasing the number of up-sampling layers from 2 to 3 almost brings no performance improvement. We hence use $L = 2$ by default.

We also include SMR ratio scaling experiments on some HumanoidBench tasks, `h1-reach-v0`, `h1-run-v0`, `h1-walk-v0`, `h1-slide-v0`. We run CIR on these tasks with the SMR ratio $M \in \{2, 4, 10\}$ for 2M environment steps. The aggregated normalized return results in Figure 10 (right) show that CIR is somewhat insensitive to M on the selected HumanoidBench tasks, despite the fact that using a larger SMR ratio M can still bring performance improvements. Notably, CIR scales the replay ratio without any need for parameter resetting tricks.

E.4 NUMERICAL RESULTS FOR ABLATION STUDIES

In this part, we list all missing detailed numerical results in our ablation study for a better understanding of the learning dynamics of all CIR variants. We present in Table 12 the detailed results of CIR variants on 7 DMC medium tasks and 7 DMC hard tasks, which correspond to the results presented in Figure 5 (left). In Table 13, we show the numerical results of the ablation study in Figure 7. In Table 14, we include the numerical results that correspond to Figure 8 in Appendix E.2.

Table 12: **Numerical results of CIR and its variants on 7 DMC medium tasks and 7 DMC hard tasks in Figure 5.** We report the average return and the standard deviations.

Task	NoTanh	NoLN	CDQ	UTD	CIR
acrobot-swingup	461.7±49.8	458.1±81.9	9.1±7.3	494.4±22.1	443.5±79.0
finger-spin	879.4±119.4	828.4±201.6	924.0±36.9	967.9±30.4	940.0±35.6
finger-turn-easy	910.0±60.3	970.1±6.2	897.7±80.0	880.9±90.3	892.5±88.9
finger-turn-hard	914.6±54.3	943.6±42.8	809.5±141.5	895.7±70.2	888.4±74.3
hopper-hop	171.0±95.6	140.2±111.3	35.1±30.8	250.1±54.7	280.1±87.9
hopper-stand	749.6±208.1	709.2±257.0	448.4±329.7	760.4±158.8	822.0±211.1
walker-run	821.0±7.4	798.8±16.6	792.8±19.9	795.2±5.5	810.0±14.0
dog-run	259.0±26.3	18.1±17.9	386.6±48.6	299.4±33.3	326.8±30.6
dog-stand	796.0±33.7	956.0±4.8	919.4±44.1	855.4±40.3	937.3±23.8
dog-trot	392.6±68.9	219.9±44.2	687.5±124.2	419.4±133.2	685.1±100.0
dog-walk	645.5±52.8	618.5±97.5	909.7±22.3	763.0±188.9	880.5±38.7
humanoid-run	175.7±19.9	129.7±14.8	1.4±0.6	162.7±31.5	174.2±22.4
humanoid-stand	838.4±37.9	761.8±103.0	583.7±337.1	785.9±84.8	846.3±35.4
humanoid-walk	618.0±64.4	536.7±22.8	550.2±53.0	520.3±39.3	528.5±18.2

Table 13: **Numerical results of CIR and its variants on 7 DMC medium tasks and 7 DMC hard tasks in Figure 7.** We report the average return and the standard deviations.

Task	ActorLN	ActorCIR	Res	NoEnt	CIR
acrobot-swingup	313.4±115.6	459.7±20.4	423.8±110.3	512.2±117.4	443.5±79.0
finger-spin	948.7±22.3	984.6±4.5	914.1±122.5	925.7±97.2	940.0±35.6
finger-turn-easy	902.8±82.7	899.4±100.5	929.6±48.7	816.1±84.4	892.5±88.9
finger-turn-hard	870.0±55.2	793.3±137.9	851.1±79.1	885.8±63.9	888.4±74.3
hopper-hop	279.9±113.8	189.8±105.0	62.2±62.5	258.2±131.7	280.1±87.9
hopper-stand	538.8±241.9	910.3±17.5	765.5±232.1	612.2±278.4	822.0±211.1
walker-run	813.9±7.4	808.1±10.0	774.8±16.3	813.0±6.3	810.0±14.0
dog-run	346.1±39.9	260.3±39.3	325.9±74.7	305.9±31.2	326.8±30.6
dog-stand	946.6±37.8	921.5±54.3	933.8±48.5	961.6±10.7	937.3±23.8
dog-trot	603.4±128.6	486.9±83.4	666.7±56.7	561.2±191.4	685.1±100.0
dog-walk	884.4±22.5	909.9±23.6	894.7±28.5	882.5±37.7	880.5±38.7
humanoid-run	148.2±11.3	177.7±27.9	162.5±18.1	135.8±7.5	174.2±22.4
humanoid-stand	592.1±87.9	811.6±37.7	770.4±103.9	799.7±61.5	846.3±35.4
humanoid-walk	593.1±108.5	477.4±88.2	538.3±47.9	490.4±46.5	528.5±18.2

Table 14: **Numerical results of CIR and its variants on 9 DMC medium tasks and 3 DMC hard tasks in Figure 8.** We report the average return and the standard deviations.

Task	NoInputLN	NoAvgRNorm	NoInputNorm	MaxRNorm	AllAvgRNorm	Orthoini	WD	AvgQ	CIR
acrobot-swingup	528.8±44.6	475.2±47.4	475.3±68.0	473.0±70.4	473.7±94.9	437.4±55.8	410.4±74.6	475.9±20.6	443.5±79.0
cheetah-run	704.0±23.6	722.5±40.5	713.7±70.4	652.4±117.8	717.4±19.7	683.1±135.1	714.9±37.2	753.6±68.8	747.0±73.2
finger-spin	867.8±125.8	970.3±15.3	954.4±16.1	975.6±14.8	962.3±23.6	967.9±23.2	974.7±16.2	969.0±27.9	940.0±35.6
finger-turn-easy	898.0±44.4	944.9±36.8	916.4±42.6	890.5±78.1	895.8±45.8	873.9±98.6	896.1±82.3	892.7±37.7	892.5±88.9
finger-turn-hard	870.1±71.0	916.6±53.1	930.2±54.2	872.4±72.6	838.2±137.0	827.4±144.7	874.6±73.0	769.2±146.2	888.4±74.3
fish-swim	778.0±23.3	742.4±25.7	784.5±19.3	758.0±20.6	733.3±43.0	768.5±29.2	739.6±44.4	768.5±29.2	781.8±21.9
hopper-hop	249.9±125.6	224.8±76.3	258.5±70.0	202.4±86.7	183.7±35.3	274.2±152.1	259.9±93.3	109.8±62.7	280.1±87.9
hopper-stand	892.0±40.4	869.4±58.0	775.0±193.9	883.9±77.5	730.8±325.3	893.1±52.8	638.2±326.8	653.1±175.2	822.0±211.1
walker-run	789.8±14.6	755.7±44.9	739.0±44.1	805.6±17.9	801.0±7.3	805.7±28.2	803.8±13.9	817.8±13.4	810.0±14.0
humanoid-run	159.8±12.1	172.3±5.5	103.9±10.1	182.5±34.1	139.0±19.2	170.6±25.4	129.5±62.6	167.1±47.4	174.2±22.4
humanoid-stand	815.3±41.0	684.0±94.0	521.2±167.2	767.5±124.0	819.0±34.4	770.7±105.8	758.8±79.2	805.8±66.0	846.3±35.4
humanoid-walk	491.5±34.7	451.5±28.7	350.4±41.5	523.3±23.5	526.4±142.7	541.7±58.3	526.4±23.0	417.7±251.0	528.5±18.2

F LEARNING CURVES

The full learning curves of CIR on DMC easy & medium tasks can be found in Figure 11, the learning curves on DMC hard tasks are shown in Figure 12, the learning curves on HumanoidBench tasks are available in Figure 13, and the learning curves on ODRL tasks are depicted in Figure 14. We also include learning curves of other baseline methods on all tasks.

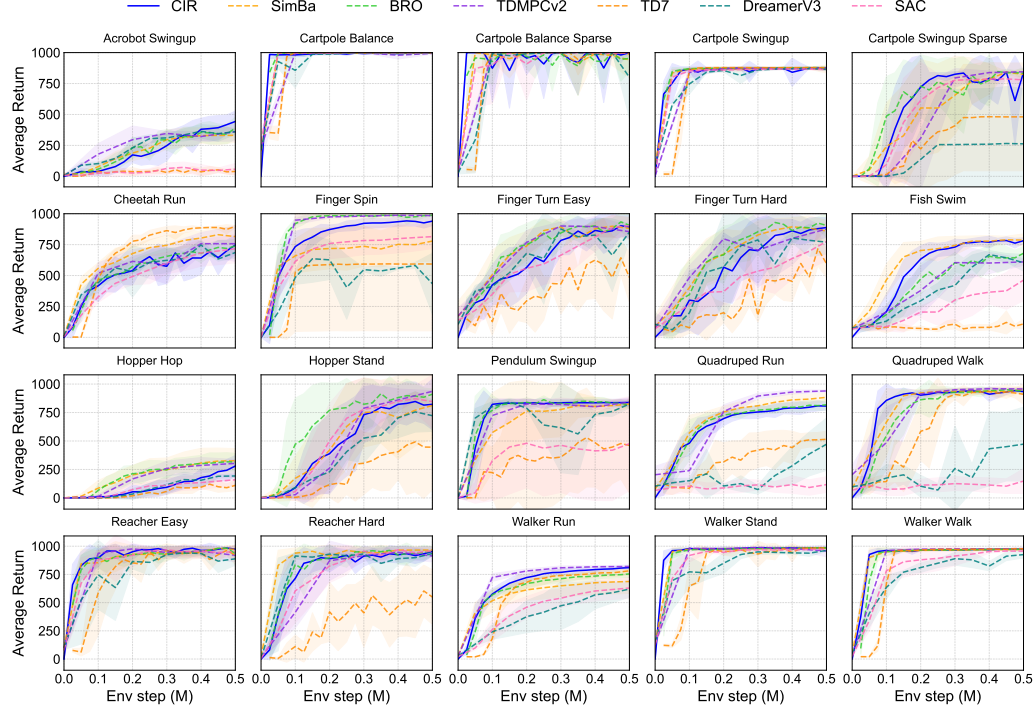


Figure 11: **Learning curves of CIR against baseline methods on DMC easy & medium tasks.** The shaded region captures the standard deviation. We run CIR for 10 random seeds.

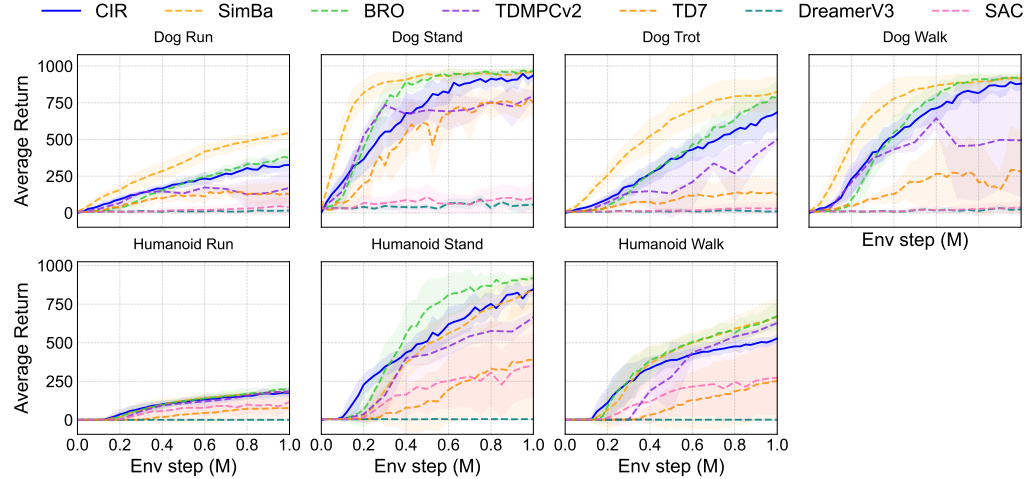


Figure 12: **Learning curves of CIR against baseline methods on DMC hard tasks.** The shaded region denotes the standard deviation. The results of CIR are averaged across 10 different random seeds.

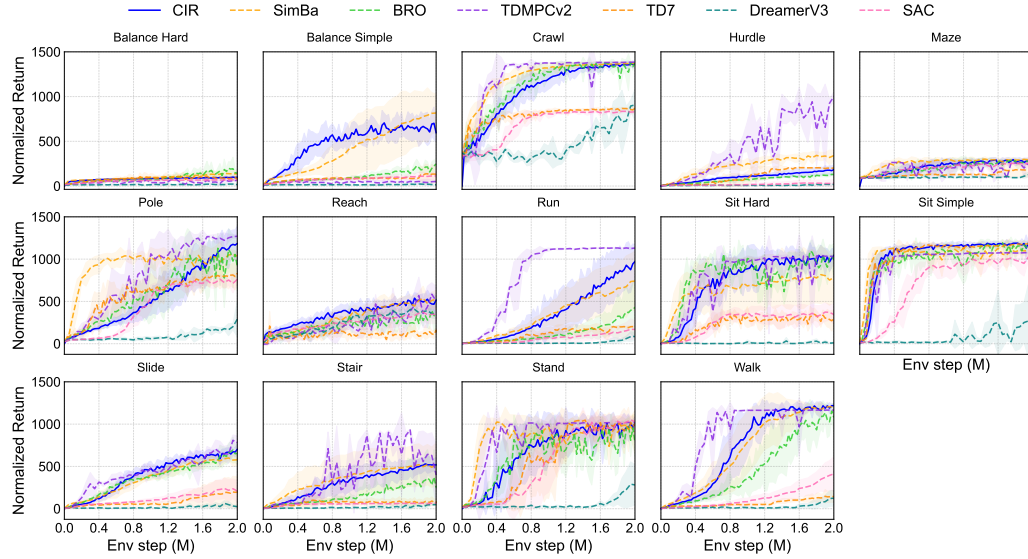


Figure 13: **Learning curves of CIR against other baseline methods on HumanoidBench tasks.** The shaded region represents the standard deviations. The results of CIR are acquired by averaging across 10 random seeds.

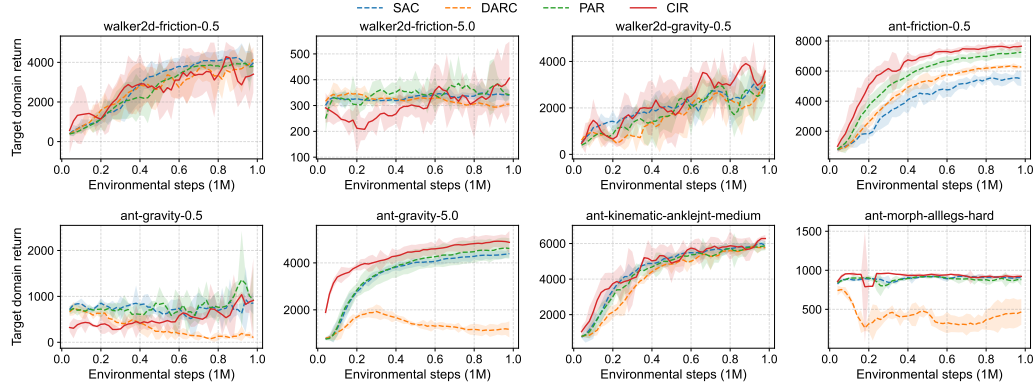


Figure 14: **Learning curves of CIR against other baseline methods on ODRL tasks.** The shaded region represents the standard deviations.

G FULL RESULTS

In this part, we include the detailed numerical results of CIR against baseline methods on each DMC task and HumanoidBench task. We report the average episode return on DMC easy & medium/hard tasks in Table 15 and Table 16, respectively, and normalized return results on HumanoidBench tasks in Table 17. Apart from the average return across all evaluated tasks, we also report statistical metrics like IQM (interquartile mean), median, and OG (optimality gap) (Agarwal et al., 2021). The results show that CIR can achieve competitive results compared to strong baselines like SimBa, TD-MPC2, and can even outperform them on some tasks.

Table 15: **Detailed results for DeepMind Control Suite Easy & Medium Tasks.** Results for CIR are averaged over 10 seeds and other results are taken directly from the SimBa paper (Lee et al., 2025a).

Task	CIR	SimBa	BRO	TD7	SAC	TD-MPC2	DreamerV3
Acrobot Swingup	443.53	331.57	390.78	39.83	57.56	361.07	360.46
Cartpole Balance	998.05	999.05	998.66	998.79	998.79	993.93	994.95
Cartpole Balance Sparse	999.60	940.53	954.21	988.58	1000.00	1000.00	800.25
Cartpole Swingup	875.22	866.53	878.69	878.09	863.24	876.07	863.90
Cartpole Swingup Sparse	839.56	823.97	833.18	480.74	779.99	844.77	262.69
Cheetah Run	747.00	814.97	739.67	897.76	716.43	757.60	686.25
Finger Spin	940.05	778.83	987.45	592.74	814.69	984.63	434.06
Finger Turn Easy	892.50	881.33	905.85	485.66	903.07	854.67	851.11
Finger Turn Hard	888.40	860.22	905.30	596.32	775.21	876.27	769.86
Fish Swim	781.79	786.73	680.34	108.84	462.67	610.23	603.34
Hopper Hop	280.10	326.69	315.04	110.27	159.43	303.27	192.70
Hopper Stand	821.98	811.75	910.88	445.50	845.89	936.47	722.42
Pendulum Swingup	837.95	824.53	816.20	461.40	476.58	841.70	825.17
Quadruped Run	807.00	883.68	818.62	515.13	116.91	939.63	471.25
Quadruped Walk	933.80	952.96	936.06	910.55	147.83	957.17	472.31
Reacher Easy	974.06	972.23	933.77	920.38	951.80	919.43	888.36
Reacher Hard	954.21	965.96	956.52	549.50	959.59	913.73	935.25
Walker Run	810.04	687.16	754.43	782.32	629.44	820.40	620.13
Walker Stand	986.66	983.02	986.58	984.63	972.59	957.17	963.28
Walker Walk	973.86	970.73	973.41	976.58	956.67	978.70	925.46
IQM	887.86	885.70	888.02	740.19	799.75	895.47	748.58
Median	840.04	816.78	836.62	623.18	676.59	836.93	684.18
Mean	839.27	823.12	833.78	636.18	679.42	836.34	682.16
OG	0.1607	0.1769	0.1662	0.3638	0.3206	0.1637	0.3178

Table 16: **Detailed results for DeepMind Control Suite Hard Tasks.** Results for CIR are averaged over 10 seeds and other results are taken directly from the SimBa paper (Lee et al., 2025a).

Task	CIR	SimBa	BRO	TD7	SAC	TD-MPC2	DreamerV3
Dog Run	326.80	544.86	374.63	127.48	36.86	169.87	15.72
Dog Stand	937.34	960.38	966.97	753.23	102.04	798.93	55.87
Dog Trot	685.11	824.69	783.12	126.00	29.36	500.03	10.19
Dog Walk	880.48	916.80	931.46	280.87	38.14	493.93	23.36
Humanoid Run	174.25	181.57	204.96	79.32	116.97	184.57	0.91
Humanoid Stand	846.25	846.11	920.11	389.80	352.72	663.73	5.12
Humanoid Walk	528.45	668.48	672.55	252.72	273.67	628.23	1.33
IQM	669.59	773.28	771.50	216.04	69.03	527.11	9.63
Median	625.85	706.39	694.20	272.62	159.36	528.26	17.13
Mean	625.52	706.13	693.40	287.06	135.68	491.33	16.07
OG	0.3745	0.2939	0.3066	0.7129	0.8643	0.5087	0.9839

Table 17: **Detailed results for HumanoidBench.** Results for CIR are averaged over 10 seeds and other results are taken directly from the SimBa paper (Lee et al., 2025a).

Task	CIR	SimBa	BRO	TD7	SAC	TD-MPC2	DreamerV3
Balance Hard	98.51	137.20	145.95	79.90	69.02	64.56	16.07
Balance Simple	597.01	816.38	246.57	132.82	113.38	50.69	14.09
Crawl	1364.81	1370.51	1373.83	868.63	830.56	1384.40	906.66
Hurdle	183.83	340.60	128.60	200.28	31.89	1000.12	18.78
Maze	286.64	283.58	259.03	179.23	254.38	198.65	114.90
Pole	1184.66	1036.70	915.89	830.72	760.78	1269.57	289.18
Reach	515.11	523.10	317.99	159.37	347.92	505.61	341.62
Run	971.70	741.16	429.74	196.85	168.25	1130.94	85.93
Sit Hard	1042.88	783.95	989.07	293.96	345.65	1027.47	9.95
Sit Simple	1197.34	1059.73	1151.84	1183.26	994.58	1074.96	40.53
Slide	701.69	577.87	653.17	197.07	208.46	780.82	24.43
Stair	517.94	527.49	249.86	77.19	65.53	398.21	49.04
Stand	1013.30	906.94	780.52	1005.54	1029.78	1020.59	280.99
Walk	1218.76	1202.91	1080.63	143.86	412.21	1165.42	125.59
IQM	809.58	747.43	558.03	256.77	311.46	885.67	72.30
Median	779.27	733.09	632.93	385.41	399.93	796.18	160.49
Mean	778.15	736.30	623.05	396.33	402.31	787.64	165.55
OG	0.3047	0.3197	0.4345	0.6196	0.6016	0.2904	0.8352

H COMPUTE INFRASTRUCTURE

In Table 18, we list the compute infrastructure that we use to run all of the algorithms.

Table 18: **Compute infrastructure.**

CPU	GPU	Memory
AMD EPYC 7452	RTX3090×8	192GB

I LIMITATIONS AND BROADER IMPACTS

Limitations. The limitations of CIR lie in three aspects: (i) CIR relies on U-shape critic networks, making it less convenient to modify the network depth compared to residual blocks; (ii) the performance of CIR is inferior to baselines on DMC hard tasks. However, CIR provides a distinct way compared to prior methods to achieve strong sample efficiency on numerous tasks with fixed algorithmic configuration and mostly fixed hyperparameters; (iii) we only evaluate CIR on several state-based online continuous control RL tasks, while the applicability of CIR on offline RL tasks or pixel-based RL tasks remains to be explored.

Broader Impacts. In this paper, we introduce a novel method called CIR to enhance the sample efficiency of off-policy RL agents. CIR successfully improves the performance of the agent by constraining its initial representations. CIR can bring new insights to the community on developing stronger and more advanced off-policy RL algorithms, and demonstrates practical potential for accelerating progress in embodied AI systems through more sample-efficient training paradigms. This work adheres to ethical AI development standards, and we have not identified significant negative societal impacts requiring special emphasis in this context.